

Global Energetics of Solar Flares. IX. Refined Magnetic Modeling

Markus J. Aschwanden

*Solar and Astrophysics Laboratory, Lockheed Martin Advanced Technology Center, Dept. ADBS, Bldg.252,
3251 Hanover St., Palo Alto, CA 94304, USA; (e-mail: aschwanden@lmsal.com)*

ABSTRACT

A more accurate analytical solution of the *vertical-current approximation nonlinear force-free field (VCA3-NLFFF)* model is presented that includes besides the radial (B_r) and the azimuthal (B_φ) magnetic field components a poloidal component ($B_\theta \neq 0$) also. This new analytical solution is of second-order accuracy in the divergence-freeness condition, and of third-order accuracy in the force-freeness condition. We re-analyze the sample of 173 GOES M- and X-class flares observed with the *Atmospheric Imaging Assembly (AIA)* and *Helioseismic and Magnetic Imager (HMI)* onboard the *Solar Dynamics Observatory (SDO)*. The new code reproduces helically twisted loops with a low winding number below the kink instability consistently, avoiding unstable, highly-twisted structures of the Gold-Hoyle flux rope type. The magnetic energies agree within $E_{VCA3}/E_W = 0.99 \pm 0.21$ with the Wiegmann (W-NLFFF) code. The time evolution of the magnetic field reveals multiple, intermittent energy build-up and releases in most flares, contradicting both the Rosner-Vaiana model (with gradual energy storage in the corona) and the principle of time scale separation ($\tau_{flare} \ll \tau_{storage}$) postulated in self-organized criticality models. The mean dissipated flare energy is found to amount to $7\% \pm 3\%$ of the potential energy, or $60\% \pm 26\%$ of the free energy, a result that can be used for predicting flare magnitudes based on the potential field of active regions.

Subject headings: Sun: Corona — Sun: Magnetic Fields

1. INTRODUCTION

How can we improve the accuracy of magnetic field measurements and the values of dissipated magnetic energies during solar flares? The *potential minimum-energy theorem* (Priest 2014; p.117) states that the potential field represents the lowest energy state of the magnetic field in the solar corona, while the free energy (defined by the difference between the potential field and the non-potential field) is the only magnetic field component that can be dissipated during solar flares and other coronal heating episodes. The free energy in active regions typically amounts to a fraction of $E_{free}/E_p \approx 1\% - 25\%$ of the potential field energy (Aschwanden et al. 2014a; Paper I). In the past, instead of calculating the free energy, the potential energy has been used to estimate the dissipated energy in solar flares (e.g., Emslie et al. 2012), which led to over-estimates of flare energies up to two orders of magnitude. Comparisons and relative magnitudes of the potential field energy E_p , the non-potential energy E_{np} , the free energy $E_{free} = (E_{np} - E_p)$, and the energy dissipated in flares E_{diss} (which can be deduced from the step-wise decrease of the free energy during a flare), have been calculated for a sample of 173 M and X-class flares in Paper I (Fig. 13 therein). These plots reveal that the dissipated flare energies are of the same magnitude as the free energies, but are far below the potential or nonpotential energy. However, many cases reveal dissipated flare energies in excess of the free energy, which is obviously unphysical, being a side-effect of an inaccurate measurement method, which is corrected in this study.

More generally, we can ask which magnetic field extrapolation model is most suitable and most accurate to measure the free energy and its evolution during flares. Traditional *non-linear force-free field (NLFFF)* codes have been found to produce large uncertainties in the horizontal (transverse to the line-of-sight) magnetic field components (e.g., Wheatland et al. 2000; Wiegelmann 2004; Wiegelmann et al. 2006; 2012), mostly due to the fact that the force-free magnetic field is extrapolated from photospheric magnetograms, although the photosphere is not force-free (Metcalf et al. 1995). Improvements have been attempted by preprocessing of the line-of-sight magnetograms by additional constraints that minimize the force-freeness and net torque balance (Wiegelmann et al. 2012), by applying a *magneto-hydrostatic (MHS)* model (Zhu et al. 2013; Wiegelmann et al. 2017; Zhu and Wiegelmann 2018), or different magnetic helicity computation methods (Thalmann et al. 2019). The magnitude of free energy in braided and twisted magnetic fields may also strongly depend on the spatial resolution (Thalmann et al. 2014) and the temporal cadence (Sun et al. 2012, 2017).

A novel method that circumvents this problem is the *Vertical-Current Approximation (VCA)* NLFFF code, which performs automated tracing of coronal loops that are used to minimize the magnetic field direction differences between the observed coronal loops (where the magnetic field is supposedly force-free) and the fitted VCA-NLFFF solutions (Aschwanden 2013a). The suitability of the VCA-NLFFF code has been proven by the fact that a step-wise decrease of the free energy in M and X-class flares has been detected in many analyzed flares (Paper I). Examples of the time evolution of the potential energy and the free energy during flares are shown in Figures 11 and 12 in Paper I, with a comparison of the NLFFF and the VCA-NLFFF calculations. Those examples confirm the compatibility of the potential energy in both the standard Wiegelmann NLFFF code and the VCA-NLFFF code. A significant stepwise decrease of the free energy is noticeable in many cases of both codes, but short-term positive increases occur also, **either due to loop twisting, a coronal illumination effect, or new emerging (current-carrying) flux**. It appears to be a property detected by the VCA-NLFFF code, since it does occur less pronounced in the Wiegelmann NLFFF code **with pre-processed data**. This raises the question what conditions affect the accuracy of reliable measurements of the free energy during flares? **Are there additional variability effects in the time evolution of the free energy ?** Is the approximation of the VCA-NLFFF code not sufficiently accurate? We will be able to answer these questions with a new version of the VCA3-NLFFF code that is based on a more accurate analytical solution. Also, the data suggest a new interpretation in terms of impulsive and intermittent vertical current injections, rather than long-term coronal storage of currents in helically twisted loops.

The content of this paper includes a more accurate analytical solution of the non-linear force free field code (VCA3-NLFFF) (Section 2), updates of the numerical code (Section 3), data analysis and results of improved magnetic energies (Section 4), a discussion of magnetic energy issues (Section 5), and conclusions (Section 6).

2. MAGNETIC FIELD MODEL

Previously we developed a nonlinear force-free field code that models the 3-D coronal magnetic field in (flaring or non-flaring) active regions, which we call the “old” Vertical-Current Approximation (VCA-NLFFF) code here (Aschwanden and Sandman 2010; Sandman et al. 2009; Sandman and Aschwanden 2011; Aschwanden et al. 2012, 2014a, 2014b, 2015b, 2016a, 2016c; 2018 Aschwanden 2013a, 2013b, 2013c, 2015, 2016b, 2019; Aschwanden and Malanushenko 2013; Warren et al. 2018). It has an advantage over other NLFFF codes by including the magnetic field of automatically traced coronal loops, while standard NLFFF

codes use the transverse field component in the non-forcefree photosphere. The inclusion of coronal field directions is accomplished by automated tracing of 2D-projected loop structures in EUV images, such as from AIA/SDO. In the following we describe the low-energy limit of the potential field, which is identical to earlier versions of the VCA-NLFFF code, and then provide a new, more accurate analytical solution for the nonpotential field, which we call the “new” Vertical-Current Approximation Version 3 (VCA3-NLFFF) code here.

2.1. Potential Field Parameterization

The conceptually simplest representation of a magnetic potential field that fulfills Maxwell’s divergence-free (solenoidal) condition ($\nabla \cdot \mathbf{B} = 0$) is a unipolar magnetic charge j that is buried below the solar surface, which predicts a spherically symmetric magnetic field $\mathbf{B}_j(\mathbf{x})$ that points away from the buried unipolar charge, and its field strength falls off with the square of the distance r_j ,

$$\mathbf{B}_j(\mathbf{x}) = B_j \left(\frac{d_j}{r_j} \right)^2 \frac{\mathbf{r}_j}{r_j}, \quad (1)$$

where B_j is the magnetic field strength at the solar surface above a buried magnetic charge, (x_j, y_j, z_j) is the subphotospheric position of the buried charge, d_j is the depth of the magnetic charge,

$$d_j = 1 - \sqrt{x_j^2 + y_j^2 + z_j^2}, \quad (2)$$

and the vector \mathbf{r}_j between an arbitrary location $\mathbf{x} = (x, y, z)$ in the solar corona (were we desire to calculate the magnetic field) and the location (x_j, y_j, z_j) of the buried charge has a distance vector \mathbf{r}_j is,

$$\mathbf{r}_j = [x - x_j, y - y_j, z - z_j]. \quad (3)$$

Of course, the concept of a magnetic charge is only valid as a far-field approximation, which avoids the complexity of the near-field details for sake of mathematical convenience. We choose a Cartesian coordinate system (x, y, z) with the origin in the Sun center and we use units of solar radii, with the direction of z chosen along the line-of-sight from Earth to Sun center. For a location near disk center ($x \ll 1, y \ll 1$), the magnetic charge depth is $d_j \approx (1 - z_j)$. Thus, the distance r_j from the magnetic charge is

$$r_j = \sqrt{(x - x_j)^2 + (y - y_j)^2 + (z - z_j)^2}. \quad (4)$$

The absolute value of the magnetic field $B_j(r_j)$ is simply a function of the radial distance r_j (with B_j and d_j being constants for a given magnetic charge),

$$B(r_j) = B_j \left(\frac{d_j}{r_j} \right)^2. \quad (5)$$

In order to obtain the Cartesian coordinates (B_x, B_y, B_z) of the magnetic field vector $\mathbf{B}_j(\mathbf{x})$, we can rewrite Eq. (1) with Eqs. (2-5) as,

$$\begin{aligned} B_x(x, y, z) &= B_j (d_j/r_j)^2 (x - x_j)/r_j \\ B_y(x, y, z) &= B_j (d_j/r_j)^2 (y - y_j)/r_j \\ B_z(x, y, z) &= B_j (d_j/r_j)^2 (z - z_j)/r_j \end{aligned} \quad (6)$$

We proceed now from a single magnetic charge to an arbitrary number N_m of magnetic charges and represent the general magnetic field with a superposition of N_m buried magnetic charges, so that the potential field can be represented by the superposition of N_m fields \mathbf{B}_j from each magnetic charge $j = 1, \dots, N_m$,

$$\mathbf{B}(\mathbf{x}) = \sum_{j=1}^{N_m} \mathbf{B}_j(\mathbf{x}) = \sum_{j=1}^{N_m} B_j \left(\frac{d_j}{r_j} \right)^2 \frac{\mathbf{r}_j}{r_j} . \quad (7)$$

The radial vector \mathbf{r}_j , the magnetic charge location (x_j, y_j, z_j) , the intersection of the vertical symmetry axis with the photosphere at (x_0, y_0, z_0) , and an arbitrary coronal location (x, y, z) are depicted in Fig. 1. The potential field of a point charge is solely defined by the radial vector component B_r (Fig. 1), by setting $B_\varphi = 0$ and $B_\theta = 0$.

2.2. Nonlinear Force-Free Field Parameterization

In order to improve the accuracy of the old VCA-NLFFF code we searched for more accurate analytical solutions of the equation system for the divergence-free,

$$\nabla \cdot \mathbf{B} = 0 , \quad (8)$$

and force-free magnetic field,

$$\nabla \times \mathbf{B} = \alpha(\mathbf{x})\mathbf{B} , \quad (9)$$

where the nonlinear force-free parameter $\alpha(\mathbf{x})$ is spatially varying, but remains constant along a given magnetic field line.

We can derive a nonlinear force-free field solution by writing the divergence-free condition (Eq. 8) and the force-free condition (Eq. 9) of a magnetic field vector $\mathbf{B} = (B_r, B_\theta, B_\varphi)$ in spherical coordinates (r, θ, φ) . The location of the magnetic charge and the spherical symmetry axis are aligned with the vertical direction to the local solar surface. Eqs. (8-9) expressed in spherical coordinates are then,

$$(\nabla \cdot \mathbf{B}) = \frac{1}{r^2} \frac{\partial}{\partial r} (r^2 B_r) + \frac{1}{r \sin \theta} \frac{\partial}{\partial \theta} (B_\theta \sin \theta) + \frac{1}{r \sin \theta} \frac{\partial B_\varphi}{\partial \varphi} = 0 , \quad (10)$$

$$[\nabla \times \mathbf{B}]_r = \frac{1}{r \sin \theta} \left[\frac{\partial}{\partial \theta} (B_\varphi \sin \theta) - \frac{\partial B_\varphi}{\partial \varphi} \right] = \alpha B_r , \quad (11)$$

$$[\nabla \times \mathbf{B}]_\theta = \frac{1}{r} \left[\frac{1}{\sin \theta} \frac{\partial B_r}{\partial \varphi} - \frac{\partial}{\partial r} (r B_\varphi) \right] = \alpha B_\theta , \quad (12)$$

$$[\nabla \times \mathbf{B}]_\varphi = \frac{1}{r} \left[\frac{\partial}{\partial r} (r B_\theta) - \frac{\partial B_r}{\partial \theta} \right] = \alpha B_\varphi . \quad (13)$$

For a simple approximative nonlinear force-free solution we require axi-symmetry with no azimuthal dependence ($\partial/\partial\varphi = 0$). This requirement simplifies Eqs. (10-13) to,

$$\frac{1}{r^2} \frac{\partial}{\partial r} (r^2 B_r) + \frac{1}{r \sin \theta} \frac{\partial}{\partial \theta} (B_\theta \sin \theta) = 0 , \quad (14)$$

$$\frac{1}{r \sin \theta} \frac{\partial}{\partial \theta} (B_\varphi \sin \theta) - \alpha B_r = 0 , \quad (15)$$

$$-\frac{1}{r} \frac{\partial}{\partial r} (r B_\varphi) - \alpha B_\theta = 0 , \quad (16)$$

$$\frac{1}{r} \frac{\partial}{\partial r}(rB_\theta) - \frac{1}{r} \frac{\partial B_r}{\partial \theta} - \alpha B_\varphi = 0 . \quad (17)$$

An approximate solution of this system of four differential equations has been analytically derived for the radial field component $B_r(r, \theta)$ (Eq. 18), the azimuthal field component $B_\varphi(r, \theta)$ (Eq. 19), and the nonlinear parameter $\alpha(r, \theta)$ (Eq. 21), for the special case of a vanishing poloidal field component $B_\theta(r, \theta) = 0$ (Aschwanden 2013a). Here we find a new (approximative) analytical solution for the poloidal field component $B_\theta(r, \theta) \neq 0$, as expressed in (Eq. 20),

$$B_r(r, \theta) = B_0 \left(\frac{d^2}{r^2} \right) \frac{1}{(1 + b^2 r^2 \sin^2 \theta)} , \quad (18)$$

$$B_\varphi(r, \theta) = B_0 \left(\frac{d^2}{r^2} \right) \frac{br \sin \theta}{(1 + b^2 r^2 \sin^2 \theta)} , \quad (19)$$

$$B_\theta(r, \theta) = B_0 \left(\frac{d^2}{r^2} \right) \frac{b^2 r^2 \sin^3(\theta)}{(1 + b^2 r^2 \sin^2 \theta)} \frac{1}{\cos \theta} , \quad (20)$$

$$\alpha(r, \theta) \approx \frac{2b \cos \theta}{(1 + b^2 r^2 \sin^2 \theta)} . \quad (21)$$

where the constant b is defined in terms of the number of full twisting turns N_{twist} over the loop length L , i.e., $b = 2\pi N_{twist}/L$. In the old VCA-NLFFF code we neglected the poloidal magnetic field component (i.e., $B_\theta = 0$), because the magnitude of this component is of second order $\propto (br \sin \theta)^2$ like the residuals of the VCA approximation. In the new VCA-NLFFF code presented here, however, we increase the accuracy of the nonpotential field solutions by taking an approximate solution of $B_\theta \neq 0$ (Eq. 20) into account. Inserting this new solution (Eqs. 18-21) into the divergence-free term (Eq. 14) and the force-free terms (Eqs. 15-17), we find that the solution is accurate to second order in $\nabla \cdot \mathbf{B}$ (Eq. 10), to third order in $[\nabla \times \mathbf{B}]_\varphi$ (Eq. 13), to fifth order in $[\nabla \times \mathbf{B}]_\theta$ (Eq. 12), and being exactly zero for the radial component $[\nabla \times \mathbf{B}]_r = 0$ (Eq. 11). A proof of this approximative analytical solution is provided in Appendix A.

2.3. Cartesian Coordinate Transformation

In the previous derivation we derived the solution in terms of spherical coordinates (r, θ, φ) in a coordinate system where the rotational symmetry axis is aligned with the vertical to the solar surface intersecting a magnetic charge j (Fig. 1), expressed with the 3-D vectors $B_r(r, \theta)$, $B_\varphi(r, \theta)$, and $B_\theta(r, \theta)$. For a model with multiple magnetic charges at arbitrary positions on the solar disk, we have to transform the individual coordinate systems $(r_j, \theta_j, \varphi_j)$ associated with magnetic charge j into a Cartesian coordinate system (x, y, z) that is given by the observers line-of-sight (in z -direction) and the observer's image coordinate system (x, y) in the plane-of-sky. The geometric relationships of the spherical coordinate vectors are shown in Fig. 1.

Defining the radial vectors \mathbf{r}_j (between (x_j, y_j, z_j) and (x, y, z)), and \mathbf{R} between the solar center $(0, 0, 0)$ and a magnetic charge (x_j, y_j, z_j) , as well as the vector products between the orthogonal spherical components $(B_r, B_\varphi, B_\theta)$, we obtain the following directional cosines of three spherical vector components (see Fig. 1),

$$\mathbf{r}_j = [x - x_j, y - y_j, z - z_j] . \quad (22)$$

$$\mathbf{R} = [x_j, y_j, z_j] , \quad (23)$$

$$\frac{\mathbf{B}_r}{B_r} = \left[\frac{x - x_j}{r_j}, \frac{y - y_j}{r_j}, \frac{z - z_j}{r_j} \right] = [\cos_{r,x}, \cos_{r,y}, \cos_{r,z}] , \quad (24)$$

$$\frac{\mathbf{B}_\varphi}{B_\varphi} = \frac{\mathbf{R} \times \mathbf{B}_r}{|\mathbf{R} \times \mathbf{B}_r|} = [\cos_{\varphi,x}, \cos_{\varphi,y}, \cos_{\varphi,z}] , \quad (25)$$

$$\frac{\mathbf{B}_\theta}{B_\theta} = \frac{\mathbf{B}_r \times \mathbf{B}_\varphi}{|\mathbf{B}_r \times \mathbf{B}_\varphi|} = [\cos_{\theta,x}, \cos_{\theta,y}, \cos_{\theta,z}] , \quad (26)$$

The vector product allows us also to extract the inclination angle θ_j between the radial magnetic field component \mathbf{B}_r and the local vertical direction \mathbf{R} ,

$$\theta_j = \sin^{-1} \left(\frac{|\mathbf{R} \times \mathbf{B}_r|}{|\mathbf{R}| |\mathbf{B}_r|} \right) . \quad (27)$$

The transformation of the non-potential field from spherical coordinates $(B_r, B_\varphi, B_\theta)$ into cartesian coordinates (B_x, B_y, B_z) , which takes the sphericity of the solar surface fully into account, amounts to

$$\begin{aligned} B_x &= B_r(r_j, \theta_j) \cos_{r,x} + B_\varphi(r_j, \theta_j) \cos_{\varphi,x} + B_\theta(r_j, \theta_j) \cos_{\theta,x} \\ B_y &= B_r(r_j, \theta_j) \cos_{r,y} + B_\varphi(r_j, \theta_j) \cos_{\varphi,y} + B_\theta(r_j, \theta_j) \cos_{\theta,y} , \\ B_z &= B_r(r_j, \theta_j) \cos_{r,z} + B_\varphi(r_j, \theta_j) \cos_{\varphi,z} + B_\theta(r_j, \theta_j) \cos_{\theta,z} \end{aligned} \quad (28)$$

This is a convenient parameterization that allows us directly to calculate the magnetic field vector of the non-potential field $\mathbf{B}_j = (B_x, B_y, B_z)$ associated with a magnetic charge j that is characterized with five parameters: $(B_j, x_j, y_j, z_j, \alpha_j)$, where the force-free α -parameter is related to the twist parameter in terms of the number of twists N_{twist} and the loop length l by $b_j = 2\pi N_{twist}/l$.

2.4. Superposition of Twisted Field Components

The total non-potential magnetic field from all $j = 1, \dots, N_m$ magnetic charges can be approximately obtained from the vector sum of all components j (in an analogous way as we applied in Eq. (7) for the potential field),

$$\mathbf{B}(\mathbf{x}) = \sum_{j=1}^{N_m} \mathbf{B}_j(\mathbf{x}) , \quad (29)$$

where the vector components $\mathbf{B}_j = (B_{x,j}, B_{y,j}, B_{z,j})$ of the non-potential field of a magnetic charge j are defined in Eq. (28), which can be parameterized with $5N_m$ free parameters $(B_j, x_j, y_j, z_j, \alpha_j)$ for a non-potential field, or with $4N_m$ free parameters for a potential field (with $\alpha_j = 0$).

Let us consider the condition of divergence-freeness. Since the divergence operator is linear, the superposition of a number of divergence-free fields is divergence-free also,

$$\nabla \cdot \mathbf{B} = \nabla \cdot \left(\sum_j \mathbf{B}_j \right) = \sum_j (\nabla \cdot \mathbf{B}_j) = 0 . \quad (30)$$

Now, let us consider the condition of force-freeness. A force-free field has to satisfy Maxwell's equation (Eq. 9). Since we parameterized both the potential field and the non-potential field with a linear sum of N_m magnetic charges, the requirement would be,

$$\nabla \times \mathbf{B} = \nabla \times \sum_{j=1}^{N_m} \mathbf{B}_j = \sum_{j=1}^{N_m} (\nabla_j \times \mathbf{B}_j) = \sum_{j=1}^{N_m} \alpha_j(\mathbf{r}) \mathbf{B}_j = \alpha(\mathbf{r}) \mathbf{B} . \quad (31)$$

Generally, these three equations of the vector $\nabla \times \mathbf{B}$ cannot be fulfilled with a scalar function $\alpha(\mathbf{r})$ for a sum of force-free field components, unless the magnetic field volume can be compartmentalized by spatially

separated sub-volumes. Since the magnetic field of each point source decreases with the square of the distance, the force-free field solution of one particular magnetic charge is not much affected by the contributions from a spatially well-separated secondary magnetic charge, and thus Eq. (31) is approximately valid for spatially well-separated sources. Our derivation of the analytical solution of the magnetic field (shown in Appendix A and summarized in Table 1) proves that the force-free condition (Eq. 31) is fulfilled with an accuracy of the third-order term of $(br \sin \theta)$. In practice, this means that the force-free field at a location with $(br \sin \theta) \leq 0.1$ has an accuracy of $(br \sin \theta) \leq 0.001$.

2.5. The Gold-Hoyle Flux Rope Test

We demonstrate the improvement of the new VCA3-NLFFF code in various ways. One test consists of calculating the figures of merit for the divergence-freeness and the force-freeness, integrated over the simulated computation box (Eqs. 48-49 in Aschwanden 2013a). Such tests yield very similar values for the old VCA-NLFFF and the new VCA3-NLFFF code. A second test is the display of poloidal field lines, which should show a curvature in poloidal planes, as it is expected for a correction from $B_\theta = 0$ to $B_\theta \neq 0$, which is indeed the case and confirms the expected change in the geometry of magnetic field lines (Fig. 2, panel b versus d).

A particularly instructive test is the reproduction of a Gold-Hoyle flux rope (Gold and Hoyle 1960), which is thought to have a large number of multiple helical windings, as inferred from eruptive flux ropes propagating along with coronal mass ejections (CMEs) through the heliosphere (Amari et al. 1996; Gibson and Low 2000; Wang et al. 2017). An attempt to reproduce such flux ropes with 1-5 full turns was carried out in Aschwanden (2013a; Appendix A), which revealed large distortions from a uniformly thick flux tube geometry (Fig. 3 left panels). With the new VCA3-NLFFF code we find that the number of helical windings does not exceed more than about one full turn (Fig. 3 right panels), no matter how large the non-potential force-free α parameter (or b) is chosen, which implies that helical geometries with more than one full turn cannot be reproduced with the new VCA3-NLFFF code. The most likely explanation for this limit is that helical magnetic field lines with a twist of more than one turn are not force-free, as it is theoretically expected from the kink instability criterion (Priest 2014; Hood and Priest 1979; Török et al. 2003; Kliem and Török 2006; Kliem et al. 2014), as well as from observational evidence ($N_{twist} \lesssim 0.5$) of the helical twisting number (or the Gauss braiding linkage number) of coronal loops in solar active regions (Aschwanden 2019). Helical flux ropes as envisioned by Gold and Hoyle (1960) may still exist in interplanetary space, but are transient and require a time-dependent solution of the non-forcefree magnetic field.

3. NUMERICAL CODE

Previously we developed the original *vertical-current approximation nonlinear force-free field code (VCA-NLFFF)* code that has been described and continuously improved over a decade (Aschwanden and Sandman 2010; Sandman and Aschwanden 2011; Aschwanden et al. 2012, 2014a, 2016a; Aschwanden 2013a, 2013b, 2013c, 2015, 2016b, 2019; Aschwanden and Malanushenko 2013; Warren et al. 2018). In the following we mention the most significant changes in the data analysis method of the new VCA3-NLFFF code only.

3.1. Improvements of the VCA3-NLFFF Code

Over the duration of the SDO mission (Pesnell et al. 2011) from 2010 to 2019, some changes in the scaling of the EUV brightness of AIA images (from a factor of unity to a factor of 0.1) occurred, which are now automatically corrected by the AIA and HMI data reading software, based on the FITS descriptor value BSCALE.

For the absolute calibration of the magnetic energy we compare the line-of-sight magnetic field component $B_z^{map}(x, y)$ of the observed HMI magnetogram with the modeled component $B_z^{model}(x, y)$ obtained from fitting each local peak in the magnetogram with the expected field from a buried unipolar magnetic charge. We obtain equivalence of the corresponding magnetic energy component for an empirical correction factor of $q_B \approx 0.8$, i.e.,

$$q_e^{model} = \frac{\sum_{x,y} (q_B \times B_z^{model})^2}{\sum_{x,y} (B_z^{map})^2}, \quad (32)$$

where the relationship $E \propto B^2$ is used for the relationship between the magnetic energy E and the magnetic field strength B . This correction factor of $q_B \approx 0.8$ accounts for missing magnetic flux in the model that results from overlapping magnetic field domains where opposite magnetic polarities (positive and negative magnetic fields) cancel out parts of the field. Note that a correction factor of $q_B = 0.8$ of the average field strength corresponds to a factor of $q_e \approx 0.8^2 = 0.64$ in magnetic energy. This correction propagates in the various forms of uncorrected magnetic energies (E_p^*, E_{np}^*) as

$$E_p(t) = E_p^*(t)/q_e^{model}, \quad (33)$$

$$E_{np}(t) = E_{np}^*(t)/q_e^{model}, \quad (34)$$

$$E_{free}(t) = E_{np}(t) - E_p(t) = [E_{np}^*(t) - E_p^*(t)]/q_e^{model}. \quad (35)$$

This empirical correction supersedes a geometric twist correction factor $q_{iso} \approx (\pi/2)^2 \approx 2.5$ used in previous work (Eq. 2 in Paper I), which represents another approach to recover under-estimated free energy.

A specialty of the VCA3-NLFFF code is the usage of EUV images (from AIA/SDO), in addition to the line-of-sight magnetograms (with $B_z(x, y)$ from HMI/SDO), in order to constrain the non-linear force-free field solution, rather than using the transverse (B_x, B_y) magnetic field components. We use AIA images in all 6 coronal wavelengths. An automated pattern recognition code, which is specialized to measure the projected 2-D coordinates $[x(s), y(s)]$ of curvi-linear features is then employed to extract coronal loop segments (mostly in the lowest density scale height of the corona) at altitudes of 2–50 Mm (see yellow curves in Figs. 4 and 5). Several hundred loop features are extracted in a set of 6 wavelength images, which are further subdivided into 7 positions per segment, and for each location the line-of-sight coordinates $z(s)$ are optimized by varying the non-linear force free α -parameter for each unipolar magnetic charge (typically 30 values $\alpha_i, i = 1, \dots, 30$).

The VCA3-NLFFF code converges to a best-fit solution of the average misalignment angle between the observed magnetic field directions and the theoretical magnetic field model for every time step (**indicated with μ_2 in Figs. 4 and 5, found in a range of $\mu_2 \approx 5.9^\circ - 20.6^\circ$ here**). The numerical convergence can be improved if the solution from a previous time step t_i is used as initial condition in the iterative convergence of subsequent time steps t_{i+1} . The convergence behavior of our VCA3-NLFFF code is found to be stable, but slightly oscillates between two subsequent time steps. In order to take advantage of this

numerical behavior, we smooth the time evolutions of the energies by averaging two subsequent solutions, which produces a smoother time evolution $E(t)$ in each of the numerically obtained energies (Eqs. 33-35),

$$E(t) = \frac{E(t_i) + E(t_{i+1})}{2}. \quad (36)$$

The most important correction of the improved VCA3-NLFFF code is the introduction of an analytical expression for the poloidal magnetic field vector $B_\theta(r, \theta)$ (Eq. 20), which was neglected in the original code, i.e., $B_\theta(r, \theta) = 0$), as well as the related coordinate transformations of the spherical magnetic field components of $\mathbf{B}_\theta(r, \theta)$ (Eq. 26) into cartesian coordinates $\mathbf{B} = (B_x, B_y, B_z)$, that depend on spherical coordinates (r, θ, φ) as derived in (Eq. 28).

4. DATA ANALYSIS AND RESULTS

We analyzed the same data set of 173 solar flares presented in Paper I, which includes all M- and X-class flares observed with the SDO (Pesnell et al. 2011) during the first 3.5 years of the mission (2010 June 1 to 2014 January 31). This selection of events has a heliographic longitude range of $[-45^\circ, +45^\circ]$, for which magnetic field modeling can be facilitated without too severe foreshortening effects near the solar limb. We use the 45-s line-of-sight magnetograms from HMI/SDO and make use of all coronal EUV channels of AIA/SDO (in the six wavelengths 94, 131, 171, 193, 211, 335 Å), which are sensitive to strong iron lines (Fe VIII, IX, XII, XIV, XVI, XVIII, XXI, XXIV) in the temperature range of $T \approx 0.6 - 16$ MK. The spatial resolution is $\approx 1.6''$ ($0.6''$ pixels) for AIA, and the pixel size of HMI is $0.5''$. The coronal magnetic field is modeled by using the line-of-sight magnetogram $B_z(x, y)$ from HMI and (automatically detected) projected loop coordinates $[x(s), y(s)]$ in each EUV wavelength of AIA. A full 3-D magnetic field model $\mathbf{B}(x, y, z)$ is computed for each time interval and flare with a cadence of 6 min (0.1 hrs), where the total duration of a flare is defined by the GOES flare start and end times, including a margin of 30 minutes before and after each flare. The size of the computation box amounts to an area with a width and length of 0.5 solar radii in the plane-of-sky, and an altitude range of 0.2 solar radius. The total number of analyzed data includes 2706 HMI images and 16,236 AIA images.

4.1. Time Evolution of Magnetic Energies

The 3-D magnetic field solutions obtained with the VCA3-NLFFF code are shown in form of magnetic field lines in Figs. 4 and 5, while we present in Figs. 6 and 7 the time evolution of the magnetic potential energy $E_p(t)$ (orange diamonds), the magnetic nonpotential energy $E_{np}(t)$ (red diamonds), the free energy $E_{free}(t)$ (red diamonds), the dissipated magnetic energy E_{diss} , and the time derivative (black hatched areas) of the GOES flux $F_{GOES}(t)$ (dashed curve), which is a proxy for the hard X-ray time profile. We compare the energies obtained with the VCA3-NLFFF code (red curves with diamonds) with those from the Wiegelmann (W-NLFFF) code (blue curves with crosses). The time evolution of the free energy $E_{free}(t)$ is computed from the cumulative negative decreases (dashed red curves) in the time interval between the flare start time and end time (black dotted lines in Figs. 6 and 7). The time intervals of negative decreases are also marked with red hatched areas in Figs. 6 and 7. Note that they often coincide with the peak time of the GOES time derivative (solid vertical black line in Figs. 6 and 7). The uncertainties of the dissipated energies E_{diss} were estimated from the median values of energy decreases in subsequent time steps.

We see different degrees of agreements between the two codes. For example, an excellent agreement between the VCA3-NLFFF and the W-NLFFF code is obtained for flare #67 (Fig. 6d), which shows a dissipated energy of $E_{diss}[\text{W-NLFFF}] = 86 \times 10^{30}$ erg, and $E_{diss}[\text{VCA3-NLFFF}] = (76 \pm 7) \times 10^{30}$ erg. In another example, the expected step function of the free energy prominently shows up in the flare #384 (Fig. 7e) with a value of $E_{diss}[\text{VCA3-NLFFF}] = (639 \pm 31) 10^{30}$ erg, but the W-NLFFF code yields a ten times smaller step with $E_{diss}[\text{W-NLFFF}] = 62 \times 10^{30}$ erg. There is one case (flare #148, Fig. 6f) with no energy decrease detected with $E_{diss}[\text{W-NLFFF}]$, while $E_{diss}[\text{VCA3-NLFFF}] = (88 \pm 12)$ shows clearly a significant magnetic energy decrease. So, there are obvious discrepancies between the W-NLFFF and the VCA3-NLFFF codes, but at this point we cannot determine which code is more accurate.

4.2. Complexity of Magnetic Field Structures

We show the forward-fitted magnetic field solutions for the 11 X-class flares (out of the 173 M- and X-class events) in Figs. 4 and 5. We see that major sunspots with opposite magnetic polarities (white and black parts of the magnetograms in Figs. 4 and 5) occur in each of the flaring active regions, but the interface between opposite magnetic polarities can be quite complex. Examples of isolated leading sunspots are observed in the flares # 66, 349, 351, and 384 (Figs. 4, 5), while the other cases manifest mixed polarity sunspots, often with sharp gradients in the magnetic field, such as in the flares #12, 147, and 148 (Figs. 4, 5). These details are important, because the degree of complexity in mixed magnetic polarities determines how well the data are suited to fit the theoretical model of buried unipolar magnetic charges. The more isolated, isotropic, and axi-symmetric a sunspot is, the better it can be fitted with a buried unipolar charge, and a higher accuracy of the fitted magnetic field strengths is expected. In other words, the sharper the magnetic field gradients become between positive and negative magnetic polarities, the less accurate is the modeling with unipolar point charges. We will come back to this issue in the next section on the accuracy of absolute magnetic field strengths.

4.3. Absolute Magnetic Field Comparison

A first quantitative test of our study is how well the VCA3-NLFFF code can retrieve the absolute magnetic field value in an active region. A widely used alternative W-NLFFF code has been created by Wiegmann et al. (2006, 2012), which we used for comparison in Paper I also. For the subset of all (11) X-class flares, a mean ratio of $E_p^{phot}/E_p^{cor} = 1.05 \pm 0.33$ was found. Here we rename the photospheric NLFFF code of Wiegmann by $E_W = E_p^{phot}$, and the coronal (vertical current approximation) code by $E_{VCA3} = E_p^{cor}$, which yields an inverse ratio of $E_{VCA3}/E_W = 0.95 \pm 0.31$ for the potential field energy. Using the improved new VCA3-NLFFF code, we find a mean ratio of

$$\frac{E_{VCA3}}{E_W} = 0.99 \pm 0.21, \quad (37)$$

for the 11 cases shown in Fig. (4-5), measured at the peak time of the free energy (which generally occurs between the flare start and flare peak in soft X-rays (as defined by GOES)). Our new result is consistent with the old results of $E_{VCA3}/E_W = 0.95 \pm 0.31$, and yields an overall mean value that is closer to unity (as expected for a perfect absolute calibration of the code), and moreover has a smaller scatter ($\sigma = \pm 0.21$) than the old code ($\sigma = \pm 0.31$). Therefore, the new VCA3-NLFFF code appears to retrieve the absolute magnetic field more accurately than the previous VCA-NLFFF code, thanks to the inclusion of the poloidal field component (B_θ) and the empirical calibration factor $q_B = 0.8$ (Eq. 32).

However, it is not entirely clear what affects the accuracy in the measurement of the magnetic field strength. Since we compare the potential field strength only, which excludes the nonlinear effects of any NLFFF code, we suspect that the accuracy is affected by the decomposition of the magnetograms into unipolar magnetic charges. For axi-symmetric magnetic field structures, such as they occur above a sunspot with spherical symmetry, the model of buried unipolar charges is expected to be most accurate. If two sunspots with opposite magnetic polarity appear to be spatially separated on the solar surface, the magnetic flux should be perfectly conserved. However, if two sunspots with opposite magnetic polarity overlap each other, part of the oppositely-directed magnetic polarity cancel out, so that the signed flux is not conserved. This interpretation predicts that the unsigned magnetic flux should be conserved for separated sunspots, while the unsigned flux is likely to be under-estimated for spatially overlapping sunspot pairs. We investigated whether systematic errors in the magnetic field reconstruction depend on the separation of the main sunspots, or on the heliographic longitude, but did not find a systematic pattern. Nevertheless, the empirical correction factor $q_e^{model} = 0.8^2 = 0.64$ (Eq. 32) for magnetic energies, which corresponds to a correction factor of $q_B^{model} = 0.8$ for magnetic fields (Eq. 32), yields a statistically accurate correction that agrees with other NLFFF codes within a few percents (Eq. 37).

4.4. Magnetic Energy Ratios

A key result of this study is the more accurate measurement of the four types of magnetic energies, i.e. the potential energy $E_p(t)$, the nonpotential energy $E_{np}(t)$, the free energy $E_{free}(t)$, and the total dissipated magnetic energy E_{diss} during a flare. As representative values we use the time averages of the potential energy,

$$E_p = \sum E_p(t)/n_t , \quad (38)$$

and the nonpotential energy,

$$E_{np} = \sum E_{np}(t)/n_t . \quad (39)$$

The free energy, which is generally defined as

$$E_{free}(t) = E_{np}(t) - E_p(t) , \quad (40)$$

contains two time-dependent components: one is the time intervals with positive increases of the free energy, and one is the time intervals with negative decreases of the free energy. We interpret the positive increases as injection of free energy from the photosphere or chromosphere (or new emerging current-carrying flux), while the negative decreases represent the dissipation of magnetic energy in the solar corona during a flare magnetic reconnection process. Thus we can define the time evolution of magnetic energy dissipation by a cumulative function that contains only time intervals with negative decreases (similar to method in Paper I),

$$E_{cum}(t_i) = E_{cum}(t_{i-1}) - ([E_{free}(t_i) - E_{free}(t_{i-1})] > 0) , \quad (41)$$

This characterization in terms of a cumulative time evolution function, which is monotonically decreasing with time, allows us to separate the internal energy dissipation from the external energy injection of additional energy. The time intervals of energy dissipation are rendered with hashed areas in the right-hand panels of Figs. (6) and (7). As representative values of the free energy we use the initial maximum of the cumulative time evolution function,

$$E_{free} = max[E_{cum}(t)] , \quad (42)$$

and as a representative value of the dissipated energy the difference between the initial maximum and the final minimum of the cumulative time evolution function,

$$E_{diss} = \max[E_{cum}(t)] - \min[E_{cum}(t)] . \quad (43)$$

This definition limits the dissipated energy to $E_{diss} \leq E_{free}$ at the upper end and to $E_{diss} > 0$ at the lower end, and therefore avoids unphysical solutions with $E_{diss} > E_{free}$.

In Fig. 8 we show the various energy correlations as a function of the potential energy (Fig. 8a,b,c) or the free energy (Fig. 8d), where we obtain the following linear regression fits in log-log space,

$$\left(\frac{E_{np}}{10^{30} \text{ erg}} \right) = 0.96 \left(\frac{E_p}{10^{30} \text{ erg}} \right)^{1.019} , \quad (44)$$

$$\left(\frac{E_{free}}{10^{30} \text{ erg}} \right) = 0.018 \left(\frac{E_p}{10^{30} \text{ erg}} \right)^{1.261} , \quad (45)$$

$$\left(\frac{E_{diss}}{10^{30} \text{ erg}} \right) = 0.0065 \left(\frac{E_p}{10^{30} \text{ erg}} \right)^{1.320} , \quad (46)$$

$$\left(\frac{E_{diss}}{10^{30} \text{ erg}} \right) = 0.43 \left(\frac{E_{free}}{10^{30} \text{ erg}} \right)^{1.044} . \quad (47)$$

These nonlinear relationships can be approximated by averaged energy ratios, for which we find the following means and standard deviations of (Fig. 8, dotted lines),

$$\left(\frac{E_{np}}{E_p} \right) \approx 1.10 \pm 0.03 , \quad (48)$$

$$\left(\frac{E_{free}}{E_p} \right) \approx 0.12 \pm 0.03 , \quad (49)$$

$$\left(\frac{E_{diss}}{E_p} \right) \approx 0.07 \pm 0.03 , \quad (50)$$

$$\left(\frac{E_{diss}}{E_{free}} \right) \approx 0.60 \pm 0.26 . \quad (51)$$

Note that the uncertainties of these energy ratios are significantly smaller than in the previous study (Paper I), which indicates less scatter due to systematic errors, especially for those with unphysical solutions $E_{diss} > E_{free}$ in the previous study. As a rule of thumb we obtain the main results that the nonpotential energy is roughly 110% of the potential energy, the free energies and dissipated energies amount typically to $\approx 10\%$ of the potential energy, and the dissipated energy is about half the free energy. These results are consistent with those in the previous study (Fig. 13 in Paper 1), but in addition display tighter correlations, smaller spreads in the energy ratios, and elimination of unphysical solutions.

4.5. Energy Closure in Flares

One of the most important tasks in our study is the energy partition and energy closure in flares. Quantitative information on different forms of energies and their partition in flares and CMEs became more available lately (Emslie et al. 2012; Warmuth and Mann 2016a, 2016b; Aschwanden et al. 2014a, 2015a,

2016a; 2017; 2019; Aschwanden 2016a, 2017; Aschwanden and Gopalswamy 2019). Virtually no statistical study on flare energies existed 5 years ago (Aschwanden 2004, 2019a). In Fig. 9 we show scatterplots of the various forms of energies as a function of the dissipated magnetic energy, which supposedly is the upper limit of any energy that can be dissipated in a flare. The panel in Fig. 9a shows a comparison between the old (VCA-NLFFF) and the new (VCA3-NLFFF) code, being a factor of 3 lower with the new code. Nevertheless, the averaged ratios of the other forms energies are all below unity, see Eqs. (48-51), which means that solar flares provide sufficient free (magnetic) energy to supply the nonthermal energy in accelerated electrons and ions, as well as direct heating and expulsion of coronal mass ejections (CMEs) (Eqs. 48-51), yielding the mean ratios,

$$\left(\frac{E_{nt,e}}{E_{diss}}\right) \approx 0.34 \pm 0.09 , \quad (52)$$

$$\left(\frac{E_{nt,i}}{E_{diss}}\right) \approx 0.11 \pm 0.03 , \quad (53)$$

$$\left(\frac{E_{dir}}{E_{diss}}\right) \approx 0.36 \pm 0.09 , \quad (54)$$

$$\left(\frac{E_{cme}}{E_{diss}}\right) \approx 0.31 \pm 0.08 . \quad (55)$$

We can (now test the energy closure by summing the primary energy release processes in E_{tot} , where the thermal energy E_{th} is defined as the sum of nonthermal heating (by electron and ion precipitation) and direct heating,

$$E_{tot} = E_{nt,e} + E_{nt,i} + E_{dir} + E_{cme} = E_{th} + E_{cme} , \quad (56)$$

for which we obtain a ratio of (Fig. 9f),

$$\left(\frac{E_{tot}}{E_{diss}}\right) = 0.79 \pm 0.12 . \quad (57)$$

A pie chart of this energy partition is shown in Fig. 10c, which significantly differs from our previous study (Fig. 10b) or the study of Emslie et al. (2012) (Fig. 10a). In Fig. 11 we depict the relative energy partitions of 12 individual flares, which have an energy closure within a factor of $1/4 \lesssim E_{tot}/E_{diss} \lesssim 4.0$. These examples document large differences between individual flares that need to be explored in more details in future studies.

4.6. Energy Size Distributions

In Fig. 12 we show the size distributions of the same 6 forms of energies as in the scatterplots of Fig. 9. Ignoring the flattening turnover at the lower side of the logarithmic size distributions, which results from undersampling of weak flares with class $M < 1.0$, all six size distributions exhibit a power law distribution $N(E) \propto E^{-\alpha}$, with a slope of $a \approx 1.6 - 1.8$, which agrees well with predictions of self-organized criticality (SOC) models. A statistical fractal-diffusive avalanche model of a slowly-driven SOC system with Euclidean dimension $S = 3$ and fractal dimension $D_S = (1 + S)/2 = 2$ predicts a power law slope of (Aschwanden 2012),

$$\alpha_P = 2 - \frac{1}{S} = \frac{5}{3} \approx 1.67 , \quad (58)$$

for the peak energy dissipation rate P , and

$$\alpha_E = 1 + \frac{(S - 1)}{(D_S + 2)} = \frac{3}{2} = 1.5, \quad (59)$$

for the dissipated energy distribution. The accuracy of the power law slope is on the order of $\sigma_\alpha \approx 0.1 - 0.2$, limited by the relatively small number of analyzed events ($N \approx 10^2$), which yields inertial ranges of 1-2 decades in the size of energies only. The values, however, are close to power law slopes in larger samples, e.g., $\alpha_E = 1.53 \pm 0.02$ for nonthermal (electron) energies in flares (Crosby et al. 1993).

5. DISCUSSION

Here we discuss some consequences of our magnetic energy measurements, which have a bearing on the capability of coronal energy storage (Section 5.1), the time scale separation of energy storage and dissipation (Section 5.2), the conservation of magnetic energy (Section 5.3), the critical twist and free energy before flaring (Section 5.4), and forecasting of the flare magnitude (Section 5.5).

5.1. Coronal Energy Storage

Since we have more accurate measurements of the time evolution of free energy, before, during, and after flares, we briefly revisit the old issue of energy storage in the solar corona. Rosner and Vaiana (1978) envisioned a unified model of cosmic flare transients, where the time evolution of energy storage and release can be derived from the event occurrence frequency distribution. Simply put, energy is stored in the solar corona with an exponential growth rate, which produces a power law distribution of flare energies, if the time intervals between two subsequent flares are governed by a stochastic (random) waiting time distribution. However, the postulated correlation between the waiting time and the intermittently released flare energies has never been confirmed by observational statistics in solar flares (Crosby et al. 1998; Wheatland 2000; Lippiello et al. 2010), and time scale arguments were brought forward that indicate that such a storage model is inconsistent with solar flare energy storage in coronal magnetic fields (Lu 1995).

If the coronal energy storage model would be true, we would expect a high level of stored free energy shortly before the flare, which then reduces to a lower level after the flare, manifesting an approximate step-function in the free energy $E_{free}(t)$. Although we do find an unambiguous step function in the free energy in some cases, with equal magnitude measured by both the W-NLFFF and VCA3-NLFFF code (e.g., flare #67 in Fig. 6d), the step-function does often not have the same magnitude in both codes (e.g., flare #384 in Fig. 7e or flare #220 in Fig. 7a), or the step function is accompanied by other impulsive magnetic energy increases after the flare peak time (e.g., flare #66 in Fig. 6c, or flare #344 in Fig. 7b). These erratic fluctuations in the free energy $E_{free}(t)$ indicate that a simple energy storage model with a monotonic increase before the flare peak, and with an irreversible decrease after the flare peak time (defined by the maximum of the GOES time derivative), is not always consistent with the observations, although we detect some level of energy decrease in all cases (Figs. 6 and 7). Consequently we should generalize the step function scenario to a more comprehensive model that allows coronal energy storage and dissipation on time scales that are even shorter than the flare duration.

We illustrate the impulsiveness of free energy storage and dissipation in Fig. 13 for the case of the longest observed flare in our sample, with a total duration of $\tau_{flare} = 4.1$ hrs. In this case we see numerous decreases

of the free energy (13 red hatched areas in Fig. 13 middle panel). Clearly the storage and dissipation of free energy varies on much shorter time scales than the flare duration, in contrast to the coronal storage model of Rosner and Vaiana (1978), where energy storage times are required to be much longer than the flare duration, continuously accumulating during two subsequent large flares (which may not repeat until time scales of days to weeks according to observations).

5.2. Time Scale Separation of Energy Storage and Dissipation

The previous discussion raises the issue of time scale separation (see also Section 2.13 in Aschwanden et al. 2016b). Self-organized criticality models assume a time scale separation between the energy build-up or storage time scale $\tau_{storage}$, and the duration τ_{diss} , i.e., $\tau_{storage} \gg \tau_{diss}$, in order to enable a slowly-driven system that produces a power law distribution of dissipated energies, as originally proposed for sandpile avalanches by Bak et al. (1987). The waiting times between subsequent avalanches are assumed to be a stochastic (random) process and to produce a Poisson distribution (Wheatland et al. 1998). The same criterion of time scale separation has been applied to the energy storage model of Rosner and Vaiana (1978), i.e., $\tau_{storage} \gg \tau_{diss}$, but the size distribution of the avalanches is assumed to follow some scaling with the waiting times, which would constitute a deterministic system, where the flare magnitude could be predicted by the waiting time, which however is not the case (see the following discussion in Section 5.5). Moreover, the time scales of energy build-up or storage, as well as the time scales of energy dissipation, are observed to be much shorter (in the order of minutes) than the flare duration (up to 4 hrs for the case shown in Fig. 13), and thus the observed time scale ranges are opposite to the model of Rosner and Vaiana (1978), as well as opposite to slowly-driven SOC models, which leaves us with “fast-driven” or “strongly-driven” SOC systems (Aschwanden et al. 2016b).

5.3. Energy Conservation During Solar Flares

Earlier estimates of flare energies assumed that the free (magnetic) energy has a high level before the flare, and then drops like a step-function to a lower level after the flare, which implies energy conservation of the free energy in the solar corona, i.e.,

$$E_{free}(t_{before}) - E_{diss} = E_{free}(t = t_{after}) . \quad (60)$$

Since we developed tools to calculate the nonpotential energy and the free energy $E_{free}(t)$ (e.g., with the W-NLFFF or VCA3-NLFFF code), we can apply the principle of energy conservation in order to determine the combined energy dissipation of the primary processes operating in flares (Eq. 56), which we estimated from the cumulative energy decrease function $E_{cum}(t)$ (by extracting it from the free energy $E_{free}(t)$ as shown in Figs. 6-7). However, since the energy dissipation often does not follow a single step-function, but rather multiple step-functions (up to ≈ 14 episodes in the long-duration flare shown in Fig. 13), we should introduce a more generalized energy conservation formalism that includes multiple step functions,

$$\sum E_{free,pos}(t)\Delta t - E_{diss} = \sum E_{free,neg}(t)\Delta t , \quad (61)$$

where $E_{free,pos}(t)$ and $E_{free,neg}(t)$ encompass time intervals with positive and negative changes of the free energy. In this study we measured the cumulative negative changes of the free energy, $E_{cum}(t) = E_{free,neg}(t)$, but did not measure the sum of the positive free energy changes, since there is some ambiguity about the flare duration and the definition of the flare-associated pre-flare and post-flare phases.

Nevertheless, our analysis indicates that the flare-associated changes of the free (magnetic) energy is often more complex than a single step-function. Moreover, since there is no simple monotonic increase of stored energy in the corona, but rather intermittent pulses of energy injection with rapid dissipation during flare phases, probably of chromospheric origin, energy conservation cannot simply be deduced from the coronal (non-potential) magnetic field alone, but has to include also energy input from the chromosphere. In this sense magnetic energy is not conserved for coronal contributions alone, but requires the knowledge of the energy contributions from the chromosphere also.

5.4. Critical Twist and Free Energy

A perhaps surprising result is the small ratio of the free magnetic energy to the potential energy, i.e., $E_{free}/E_p = 0.12 \pm 0.03$ (Fig. 8b; Eq. 49). Why is the available free energy an order of magnitude smaller than the total potential field energy? According to the helically twisted geometry of a flux tube, this energy ratio can be translated into a geometric angle between the potential and nonpotential field components, which is also known as helical (or azimuthal) twist angle,

$$\frac{E_{free}}{E_p} = \frac{B_\phi^2}{B_p^2} = (\tan \mu)^2. \quad (62)$$

According to our measurements with $E_{free}/E_p \approx 0.12 \pm 0.03$, the energy ratio corresponds to a helical twist angle of

$$\mu = \arctan \left[\left(\frac{E_{free}}{E_p} \right)^{1/2} \right], \quad (63)$$

yielding a value of $\mu = 19^\circ \pm 2^\circ$. Thus we suspect that helical twisting is occurring until a critical angle of $\mu_{crit} \approx 19^\circ$ is reached, while further accumulation of free energy by helical twisting is inhibited by some stabilizing force, or by the onset of an instability.

The number of twisting turns in a flux tube can be expressed by

$$\tan \mu = \frac{N_{twist} 2\pi r}{L} \approx 6.3 N_{twist} \left(\frac{r}{L} \right). \quad (64)$$

where r is the flux tube radius and L is the loop length. For instance, a critical twist angle of $\mu = 19^\circ$ and an aspect ratio of $(r/L) = (1/20)$ yields a number of one twist turn, i.e., $N_{twist} \approx 1.0$, which is the approximate threshold for the kink instability (Priest 2014; Hood and Priest 1979; Török et al. 2003; Kliem and Török 2006; Kliem et al. 2014). Hence, a constant value of the critical helical twist angle can explain the proportionality between the free energy E_{free} and the potential energy E_p found here (Eq. 49), as well as the prediction that the free energy scales with the helical twist angle μ (Eq. 63).

5.5. Flare Magnitude Prediction

The performance of solar flare forecasting methods has been diligently tested, but there is no consensus about the best method (Schrijver 2007; Georgoulis and Rust 2007; Leka and Barnes 2003; Barnes et al. 2007, 2016; Barnes and Leka 2008; Bloomfield et al. 2012; Colak and Qahwaji 2009; Li et al. 2007; Ahmed et al. 2013; Falconer et al. 2003, 2011, 2012; Mason and Hoeksema 2010; Cui et al. 2006; Bobra and Itonidis 2016; Nishizuka et al. 2017; Jonas et al. 2018; Bélanger et al. 2007; Strugarek and Charbonneau 2014). A question

of general interest is whether the evolution of the free energy, $E_{free}(t)$ can be used for flare forecasting? The free energy has been found to be one of the best correlated flare indicators (Bobra and Couvidat 2015). However, the free energy calculated in Bobra and Couvidat (2015) is derived from photospheric magnetograms, which measure the longitudinal (line-of-sight) component B_z and the transverse components B_x and B_y in the non-forcefree photosphere (Metcalf et al. 1995). Another well-correlated parameter that can be calculated with our VCA3-NLFFF code includes the total unsigned vertical current.

Our statistics with enhanced accuracy provides some useful information for forecasting of the magnitude of solar flares. The tight correlations between the four magnetic energy parameters found here (i.e., the potential, non-potential, free energy, and flare-dissipated energies) (Fig. 8) enables us to predict the flare magnitude from the knowledge of the potential field of an active region. The potential field is easy to calculate and is slowly-varying in an active region, often being stable over several days (Sun et al. 2012). From another statistical study it was concluded that currents associated with coronal nonpotentiality have a characteristic growth and decay time scale of $\approx 10 - 30$ hrs (Schrijver et al. 2005; Schrijver 2016). The free energy is confined to a relative small fraction of $12\% \pm 3\%$ of the potential energy (Eq. 49). Also the flare-dissipated energy is found in a relatively small range of $7\% \pm 3\%$ (Eq. 50), from which we can predict an upper limit of the dissipated energy a few days ahead of the flare. We can not predict the specific onset time of the flare, but we can provide an upper limit of the largest flare occurring the next few days. The uncertainty of our prediction method, based on the statistical ratio found here for M- and X-class flare events, i.e., $E_{diss}/E_p = 7\% \pm 3\%$ (Eq. 50), amounts to a factor of $10\%/7\% = 1.4$. The largest nonpotential energy we measured in this study is $E_{np} \approx 6 \times 10^{33}$, from which we predict a maximum dissipated flare energy of $7\% \pm 3\%$, or $E_{diss} = 4.2 \pm 1.8 \times 10^{32}$ erg, similar to our actual measurement of $E_{diss}^{obs} = 6.4 \times 10^{32}$ erg (Table 2).

6. CONCLUSIONS

In this study and in Paper I we follow the approach of modeling the magnetic energies in flaring active regions by calculating approximative analytical solutions of non-linear force-free fields in terms of the vertical-current approximation, using the observational data of projected coordinates $[x(s), y(s)]$ of (automatically traced) coronal loops from EUV (AIA/SDO) images, and the line-of-sight component $B_z(x, y)$ from photospheric (HMI/SDO) magnetograms. In Paper I we derived an analytical solution of the magnetic field components $[B_r(\mathbf{x}), B_\varphi(\mathbf{x})]$ in spherical coordinates $[r, \varphi, \theta]$, neglecting the poloidal field component ($B_\theta(\mathbf{x}) = 0$). In this Paper IX, we refine the analytical solution by including a solution of the poloidal field component ($B_\theta(\mathbf{x}) \neq 0$), which yields more accurate values of the magnetic field $\mathbf{B}(\mathbf{x}, \mathbf{t})$ and (non-potential) magnetic energies $E_{np}(\mathbf{x}, \mathbf{t})$. The new analytical solution, which is calculated with the VCA3-NLFFF code, is of second-order accuracy in the divergence-freeness condition, and of third-order accuracy in the force-freeness (or solenoidal) condition. The main new results and conclusions are:

1. **The Gold-Hoyle flux rope test:** Highly twisted flux ropes with a large number of helical windings are thought to drive the expulsion of coronal mass ejections from a coronal flare site out to the heliosphere (Gold and Hoyle 1960). Such a highly twisted structure with 5 windings could be reproduced with the old VCA-NLFFF code (Aschwanden 2013a), while the new VCA3-NLFFF code could only produce magnetic field lines with less than a half winding turn (Aschwanden 2019), but this inability is consistent with the expected non-existence of nonlinear force-free field solutions at $N_{twist} \gtrsim 1$ due to the kink instability criterion. However, such Gold-Hoyle structures may exist as transients in

interplanetary space, where force-freeness is not required.

2. **Accuracy of the VCA3-NLFFF code:** The accuracy of a magnetic field measurement $\mathbf{B}(\mathbf{x})$ with the VCA3-NLFFF code is limited in zones where magnetic concentrations with opposite magnetic polarity overlap, so that the signed magnetic flux partially cancels out. We find that this results into an underestimate of the magnetic field by a statistical factor of $q_B \approx 0.8$. Correcting for this statistical factor yields an agreement of the magnetic (nonpotential) energy within a mean and standard deviation of $E_{VCA3}/E_W = 0.99 \pm 0.21$ with respect to the Wiegelmann (W-NLFFF) code.
3. **Time evolution of the magnetic field:** In the simplest concept we would expect that the free energy has a steady, relatively high value before a flare, then decreases like a step-function, and reaches a relatively low value after the flare. While this single step-function scenario approximates the measured free energy $E_{free}(t)$ quite well in some cases, the detailed evolution of the free energy exhibits multiple short-term increases, followed by decreases on time scales that are shorter than the flare duration, up to 13 such episodes during a (≈ 4 hour) long-duration flare. The energy evolution during flares thus exhibits an intermittent and impulsive behavior of energy build-up and dissipation that is more complex than a single step-function.
4. **Magnetic energy ratios:** Defining a cumulative (monotonically decreasing) function of negative energy steps during the flare duration, we obtain a measure for the evolution of the free energy $E_{free}(t)$ during a flare, bound by the energy difference between the flare start and end. We find that the dissipated energy amounts to a statistical ratio of $E_{diss}/E_{free} = 0.60 \pm 0.26$ with respect to the free energy, or $E_{diss}/E_p = 0.07 \pm 0.03$ with respect to the potential energy of a flaring active region. The latter ratio is useful for predicting upper limits of flare energies.
5. **Energy closure:** The total dissipated energy in a flare (E_{tot}) is converted into nonthermal energy of accelerated electrons ($E_{nt,e}$) and ions ($E_{nt,i}$), direct heating of coronal plasma (E_{dir}), and possible launch of a CME (E_{cme}), which can be expressed also by the sum of the thermal energy E_{th} (in a secondary energy conversion step) and the kinetic CME energy E_{cme} . We find an energy closure of $E_{tot}/E_{diss} = 0.79 \pm 0.12$, which compares favorably with earlier work, i.e., $E_{tot}/E_{diss} = 0.87 \pm 0.18$ (Aschwanden et al. 2017; Paper V). The energy closure in individual events, however, varies by a much larger factor, which indicates large uncertainties in individual energy measurements that need to be investigated in further detail.
6. **Coronal energy storage:** The intermittent and impulsive behavior of the time evolution of the free energy $E_{free}(t)$ contradicts the single-step energy dissipation scenario of Rosner and Vaiana (1978). We find up to 14 episodes of consecutive free energy increases and decreases in a (4-hour long-duration) flare event, with a cadence (of 6 min) that is only a factor 3 shorter than the mean period of the free energy fluctuations. Long-duration energy storage with a singular energy dissipation phase thus cannot explain the observed time variability of the free energy.
7. **Time scale separation:** The increase of free energy in a flaring region, which is expected over a relatively long duration (compared with the flare duration), is found to fluctuate almost erratically before, during, and after flares. These short-term fluctuations thus violate the time scale separation $\tau_{flare} \ll \tau_{storage}$, which is also expected in slow-driven self-organized criticality (SOC) models, and instead require a “fast-driven” or “strongly-driven” model (Aschwanden et al. 2016b), which might produce significant deviations from power law size distribution. The size distributions observed here, however, preserve the power law distribution and match the predicted slopes of $\alpha \approx 1.5 - 1.7$ (Fig. 12).

8. **Energy conservation:** The simple step-function scenario of coronal energy build-up and dissipation implies energy conservation of the coronal magnetic field, where the free energy before a flare matches the free energy after the flare plus the amount of dissipated energy associated with the primary energy conversion processes (Eq. 56). The mismatch of the single step-function scenario, however, suggests that energy is externally injected into the coronal flare region (such as vertical currents from the chromosphere), in an intermittent way, since the storage process seems to be independent of the dissipation process. Consequently, energy conservation during flares requires the knowledge of external energy injections also.
9. **Critical twist and kink instability:** Fitting the vertical-current approximation NLFFF model to coronal loops yields the ratio of the helically twisted azimuthal magnetic field component $B_\varphi(\mathbf{x})$ to the potential radial field component $B_r(\mathbf{x})$, which implies a helical twist angle of $\mu = 19^\circ \pm 2^\circ$ in our data, or a winding number of $N_{twist} \lesssim 0.5$ (Aschwanden 2019b). This relatively low value is also compatible with the critical twist angle or threshold of the kink instability at $N_{twist} \gtrsim 1.0$ (Tóroek et al. 2003). This instability limit sets also an upper limit for the ratio of the free energy to the potential free energy, and this way constrains a useful criterion for the prediction of flare magnitudes.
10. **Flare magnitude prediction:** We found tight correlations between the (potential, non-potential, free, and dissipated) magnetic energy parameters. The mean ratio between the dissipated flare energy E_{diss} and the potential energy E_{free} , for instance, has a relatively narrow ratio of $E_{diss}/E_p = 0.07 \pm 0.03$, which implies a standard deviation by a factor of 1.4 only. Since the potential energy of an active region is generally slowly-varying over the course of a few days, $E_p(t)$ is almost constant (Sun et al. 2012), and upper limits $E_{diss} \lesssim (0.07 \pm 0.03) \times E_p$ can be predicted for any flare a few days ahead.

We carried out magnetic modeling with both the VCA-NLFFF and the W-NLFFF code, in both Paper I and in this present study (Paper IX). The comparisons help us to better understand the absolute and relative uncertainties. It is gratifying to see that we obtain relatively consistent results, regardless whether we use transverse magnetic field components (B_x, B_y) (W-NLFFF) or loop coordinates $[x(s), y(s)]$ (VCA-NLFFF). Theoretically, the VCA-NLFFF code is preferable because it circumvents the non-forcefreeness issue in the photosphere (Metcalf et al. 1995; DeRosa et al. 2009), and instead uses geometric constraints of coronal loops, while the W-NLFFF code executes coronal field extrapolations rooted in photospheric non-forcefree fields. Future magnetic field computation methods may combine the advantages of both types of codes.

The author thanks for helpful discussions with Marc DeRosa, John Serafin, and Wei Liu. Part of the work was supported by NASA contract NNG 04EA00C of the SDO/AIA instrument and the NASA STEREO mission under NRL contract N00173-02-C-2035.

APPENDIX A

In this Appendix A we derive our new analytical solution of a divergence-free and force-free magnetic field (used in the new VCA3-NLFFF code), which represents a more accurate solution than the original approximation derived in Aschwanden (2013a), where the poloidal magnetic field component was neglected, i.e., $B_\theta = 0$. Thus we start from the original approximation (Eqs. A1, A2, A3, A4),

$$B_r(r, \theta) = B_0 \left(\frac{d^2}{r^2} \right) \frac{1}{(1 + b^2 r^2 \sin^2 \theta)}, \quad (A1)$$

$$B_\varphi(r, \theta) = B_0 \left(\frac{d^2}{r^2} \right) \frac{br \sin \theta}{(1 + b^2 r^2 \sin^2 \theta)}, \quad (\text{A2})$$

$$B_\theta(r, \theta) \approx 0, \quad (\text{A3})$$

$$\alpha(r, \theta) \approx \frac{2b \cos \theta}{(1 + b^2 r^2 \sin^2 \theta)}. \quad (\text{A4})$$

where the constant b is defined in terms of the number of full twisting turns N_{twist} over the loop length L , i.e., $b = 2\pi N_{twist}/L$. From the second equation of the forcefree condition (Eq. 16) we can express the poloidal field component explicitly,

$$B_\theta(r, \theta) = -\frac{1}{r\alpha} \frac{\partial}{\partial r} (rB_\varphi), \quad (\text{A5})$$

where we can insert the azimuthal field component $B_\varphi(r, \theta)$ (Eq. A2), the nonlinear α -parameter, $\alpha(r, \theta)$ (Eq. A4), calculate the radial derivative $\partial(rB_\varphi)/\partial r$, and obtain this way an explicit expression for the poloidal field component,

$$B_\theta(r, \theta) = B_0 \left(\frac{d^2}{r^2} \right) \frac{b^2 r^2 \sin^3(\theta)}{(1 + b^2 r^2 \sin^2 \theta) \cos \theta}. \quad (\text{A6})$$

which represents a more accurate approximation than the original approximation with $B_\theta = 0$. For numerical calculations we find that the expression (A6) is numerically unstable, but can be fully stabilized by approximating the cosine term with $\cos(\theta) = 1$, without losing significant accuracy.

A second task is the accuracy of the divergence-free condition (Eq. 10), which for axi-symmetric fields ($\partial/\partial\varphi = 0$) reduces to Eq. (14),

$$\frac{1}{r^2} \frac{\partial}{\partial r} (r^2 B_r) + \frac{1}{r \sin \theta} \frac{\partial}{\partial \theta} (B_\theta \sin \theta) = 0. \quad (\text{A7})$$

We can insert the expressions for the radial magnetic field component $B_r(r, \theta)$ (Eq. A1), the poloidal magnetic field component $B_\theta(r, \theta)$ (Eq. A6), and calculate the derivatives $\partial(r^2 B_r)/\partial r$ and $\partial(B_\theta \sin \theta)/\partial \theta$, which after some lengthy algebra leads to the expression,

$$\nabla \cdot \mathbf{B} = \frac{B_0 d^2}{r^3} \left[\frac{2b^2 r^2 \sin^2 \theta \cos^2 \theta + b^2 r^2 \sin^4 \theta - 2b^4 r^4 \sin^4 \theta \cos^2 \theta + b^4 r^4 \sin^6 \theta}{\cos^2 \theta (1 + b^2 r^2 \sin^2 \theta)^2} \right] \approx \left(\frac{B_0 d^2}{r^3} \right) O(br \sin \theta)^2, \quad (\text{A8})$$

which is of second-order in the argument ($br \sin \theta$), similar to the original approximation (Aschwanden 2013a). This means that the approximation is most accurate for a weakly nonlinear forcefree magnetic fields with $(br \sin \theta) \ll 1$ or $\alpha \ll 1$. Note that the divergence of the potential field can be obtained from Eq. (A8) by setting $b = 0$,

$$\nabla \cdot \mathbf{B} = \left(\frac{B_0 d^2}{r^3} \right) \times O = 0. \quad (\text{A9})$$

A next task is the assessment of the accuracy of the force-free condition (Eq. 9 or 11-13). For the radial component $[\nabla \times \mathbf{B}]_r$ (Eq. 11), and applying axi-symmetry ($\partial/\partial\varphi = 0$), Eq. 11 reduces to,

$$[\nabla \times \mathbf{B}]_r = \frac{1}{r \sin \theta} \left[\frac{\partial}{\partial \theta} (B_\varphi \sin \theta) \right] = \alpha B_r. \quad (\text{A10})$$

Inserting the azimuthal field component $B_\varphi(r, \theta)$ (A2) and calculating the derivative $\partial\theta(B_\varphi \sin \theta)/\partial\theta$, we find that all terms in this expression cancel out, so that this forcefree condition is exactly fulfilled,

$$[\nabla \times \mathbf{B}]_r = 0, \quad (\text{A11})$$

which was also the case in the old VCA-NLFFF code, as given in Aschwanden (2013a). The second vector component of the forcefree condition, i.e., $[\nabla \times \mathbf{B}]_\theta$ (Eq. 12), with axi-symmetry applied ($\partial/\partial\varphi = 0$), simplifies to

$$[\nabla \times \mathbf{B}]_\theta = - \left[\frac{1}{r} \frac{\partial}{\partial r} (r B_\varphi) \right] = \alpha B_\theta . \quad (A12)$$

Inserting the magnetic field components $B_\varphi(r, \theta)$ (Eq. A2), $B_\theta(r, \theta)$ (Eq. A6), the nonlinear parameter $\alpha(r, \theta)$ (Eq. A4), and calculating the derivative $\partial(r B_\varphi)/\partial r$ yields then the expression,

$$[\nabla \times \mathbf{B}]_\theta = \left(B_0 \frac{d^2}{r^3} \right) \frac{(-2b^5 r^5 \sin^5 \theta)}{(1 + b^2 r^2 \sin^2 \theta)^2} \approx \left(\frac{B_0 d^2}{r^3} \right) O(br \sin \theta)^5 , \quad (A13)$$

which is of fifth-order accuracy in the argument ($br \sin \theta$).

Finally we assess the accuracy of the third vector component of the forcefree condition, $[\nabla \times \mathbf{B}]_r$ (Eq. 11). The axi-symmetry $\partial/\partial\varphi = 0$ simplifies the expression Eq (11) to,

$$[\nabla \times \mathbf{B}]_r = \frac{1}{r \sin \theta} \left[\frac{\partial}{\partial \theta} (B_\varphi \sin \theta) \right] = \alpha B_r , \quad (A14)$$

Inserting the magnetic field components $B_\varphi(r, \theta)$ (Eq. A2), the radial component $B_r(r, \theta)$ (Eq. A1), the nonlinear parameter $\alpha(r, \theta)$ (Eq. A4), and calculating the derivative $\partial(B_\varphi \sin \theta)/\partial \theta$ yields then an expression where all terms cancel out,

$$[\nabla \times \mathbf{B}]_r = 0 , \quad (A15)$$

as they cancelled out in the old approximation with $B_\theta = 0$ also.

We list an overview of the accuracy orders of these approximations in Table 1. In the overall, the lowest order among all components is of second order, in both the old and the new (VCA3-NLFFF) codes, but the poloidal force-free component $[\nabla \times \mathbf{B}]_\theta$ improved from third-order to fifth-order, mostly due to the more accurate approximation of $B_\theta \neq 0$ (A6).

Table 1: Order of Accuracy in the Divergence-Freeness and Force-Freeness Conditions in the Analytical Approximation of the (Old) VCA-NLFFF and (New) VCA3-NLFFF Code.

Equation	Old code VCA-NLFFF	New code VCA3-NLFFF
$\nabla \cdot \mathbf{B}$	$(br \sin \theta)^2$	$(br \sin \theta)^2$
$[\nabla \times \mathbf{B}]_r$	0	0
$[\nabla \times \mathbf{B}]_\theta$	$(br \sin \theta)^3$	$(br \sin \theta)^5$
$[\nabla \times \mathbf{B}]_\varphi$	0	$(br \sin \theta)^3$

Table 2: Energy parameters of the first 10 out of the 174 M- and X-class flare events in the longitude range of $[-45^\circ, +45^\circ]$, computed with the new VCA3-NLFFF Code. The full Table can be downloaded electronically from the journal as a machine-readable ASCII file.

Nr	Date	Time	GOES	Helio	E_p	E_{np}	E_{free}	E_{diss}	$E_{nt,e}$	$E_{nt,i}$	E_{dir}	E_{th}	E_{cme}	E_{sum}
3	2010-08-07	17:55	M1.0	N13E34	402.2	459.5	59.5	22.4	1.1	0.4	6.8	8.2	0.0	8.2
4	2010-10-16	19:07	M2.9	S18W26	164.6	173.6	12.7	11.7	1.4	0.5	17.4	19.2	0.1	19.3
10	2011-02-13	17:28	M6.6	S21E04	802.3	866.0	66.5	23.8	6.8	2.3	11.6	20.8	0.7	21.4
11	2011-02-14	17:20	M2.2	S20W07	998.6	1058.6	71.4	35.3	0.0	0.0	13.5	13.5	0.5	13.9
12	2011-02-15	01:44	X2.2	S21W12	966.8	1039.2	94.1	38.8	25.1	8.5	48.6	82.2	9.7	91.9
13	2011-02-16	01:32	M1.0	S22W27	959.2	1037.1	101.8	79.2	2.5	0.9	3.9	7.3	2.0	9.3
14	2011-02-16	07:35	M1.1	S23W30	1100.3	1209.6	125.0	59.8	0.0	0.0	4.4	4.4	0.0	4.4
15	2011-02-16	14:19	M1.6	S23W33	1054.5	1163.8	146.2	89.5	4.6	1.6	0.2	6.4	0.0	6.4
16	2011-02-18	09:55	M6.6	N15E05	727.3	779.1	87.3	83.1	11.8	4.0	0.1	4.2	0.0	15.9
17	2011-02-18	10:23	M1.0	N17E07	743.3	808.5	70.5	8.9	0.0	0.0	3.4	3.4	0.0	3.4

REFERENCES

- Ahmed, O.W., Qahwaji, R., Colak, T., et al. 2013, SoPh 283, 157
- Amari, T., Luciani, J.F., Aly, J.J., and Tagger, M. 1966, ApJ 466, L39
- Aschwanden, M.J., 2004, *Physics of the Solar Corona. An Introduction*, Praxis and Springer, Berlin, 216.
- Aschwanden, M.J. and Sandman, A.W. 2010, AJ 140, 723
- Aschwanden, M.J. 2012, A&A 539, A2
- Aschwanden, M.J., Wuelser, J.P., Nitta, N.V., Lemen, J.R., Schrijver, C.J., et al. 2012, ApJ 756, 124
- Aschwanden, M.J. 2013a, SoPh 287, 323
- Aschwanden, M.J. 2013b, SoPh 287, 369
- Aschwanden, M.J. 2013c, ApJ 763, 115
- Aschwanden, M.J. and Malanushenko, A. 2013, SoPh 287, 345
- Aschwanden, M.J., Xu, Y., and Jing J. 2014a, ApJ 797:50, (Paper I)
- Aschwanden, M.J., Sun, X.D., and Liu, Y. 2014b, ApJ 785, 34
- Aschwanden, M.J. 2015, ApJ 804, L20
- Aschwanden, M.J., Boerner, P., Ryan, D., Caspi, A., McTiernan, J.M., and Warren, H.P. 2015a, ApJ 802, 53, (Paper II)
- Aschwanden, M.J., Schrijver, C.J., and Malanushenko, A. 2015b, SoPh 290, 2765
- Aschwanden, M.J. 2016a, ApJ 831, 105, (Paper IV).
- Aschwanden, M.J. 2016b, ApJSS 224, 25
- Aschwanden, M.J., O’Flannagain, A., Caspi, A., McTiernan, J.M., Holman, G., et al. 2016a, ApJ 832, 27, (Paper III)
- Aschwanden, M.J., Crosby, N.B., Dimitropoulou, M., et al. 2016b, SSRv 198:47
- Aschwanden, M.J., Reardon, K., and Jess, D. 2016c, ApJ 826, 61
- Aschwanden, M.J., Caspi, A., Cohen, C.M.S., Holman, G.D., Jing, J., et al. 2017, ApJ 836, 17, (Paper V)
- Aschwanden, M.J. 2017, ApJ 847, 27, (Paper VI).
- Aschwanden, M.J., Gosic, M., Hurlburt, N.E., and Scullion, E. 2018, ApJ 866, 72 (VCA)
- Aschwanden, M.J. and Gopalswamy, N. 2019, ApJ 877, 149, Paper VII
- Aschwanden, M.J., Kontar, E.P., and Jeffrey, N.L.S. 2019, ApJ 881:1, (Paper VIII)
- Aschwanden, M.J. 2019a, *New Millennium Solar Physics*, Springer Nature, Switzerland, Science Library Vol. 458
- Aschwanden, M.J. 2019b, ApJ 874, 131
- Bak, P., Tang, C., and Wiesenfeld, K. 1987, PhRvL 59/4, 381.

- Barnes, G., Leka, K.D., Schumer, E.A., et al. 2007, *Space Weather* 5/9, S09002
- Barnes, G. and Leka, K.D. 2008, *ApJ* 688, L107
- Barnes, G., Leka, K.D., Schrijver, C.J., et al. 2016, *ApJ* 829, 89
- Bélanger, E., Vincent, A., and Charbonneau, P. 2007, *SoPh* 245, 141
- Bloomfield, D.S., Higgins, P.A., McAteer, R.T.J., et al. 2012, *ApJ* 747, L41
- Bobra, M.G. and Couvidat S. 2015, *ApJ* 798, 125
- Bobra, M.G. and Ilonidis, S. 2016, *ApJ* 821, 127
- Colak, T. and Qahwaji, R. 2009, *Space Weather* 7/6, S06001.
- Crosby, N.B., Aschwanden, M.J., and Dennis, B.R. 1993, *SoPh* 143, 275.
- Crosby, N.B., Vilmer, N., Lund, N., and Sunyaev, R. 1998, *A&A* 334, 299
- Cui, Y., Li, R., Zhang, L. et al. 2006, *SoPh* 237, 45
- DeRosa, M.L., Schrijver, C.J., Barnes, G., Leka, K.D., Lites, B.W., Aschwanden, M.J., et.al. 2009, *Apj* 696, 1780
- Emslie, A.G., Dennis, B.R., Shih, A.Y., Chamberlin, P.C., Mewaldt, R.A., Moore, C.S. et al. 2012, *ApJ* 759, 71
- Falconer, D.A., Moore, R.L., and Gary, G.A. 2003, *JGR* 108, A10, 1380
- Falconer, D.A., Abdunnasser, F., Khazanov, I., et al. 2011, *Space Weather* 9/4, S04003
- Falconer, D.A., Moore, R.L., Barghouty, A.F., et al. 2012, *ApJ* 757, 32
- Georgoulis, M.K. and Rust, D.M. 2007, *ApJ* 661, L109
- Gibson, S.E. and Low, B.C. 2000, *JGR* 105/A8, 18187
- Gold, T. and Hoyle, F. 1960, *MNRAS* 120/2, 89.
- Hood, A.W. and Priest, E.R. 1979, *SoPh* 64, 303
- Jonas, E., Bobra, M., Shankar, V., et al. 2018, *SoPh* 293, 48
- Kliem, B. and Török, T. 2006, *Phys.Rev.Let.* 96/25, 255002
- Kliem, B., Lin, J., Forbes, T.G., Priest, E.R., and Török, T. 2014, *ApJ* 789, 46
- Leka, K.D. and Barnes, G. 2003, *ApJ* 595, 1277
- Li, R., Wang, H.N., He, H. et al. 2007, *Chinese J. Astron.Astrophys.* 7/3, 441
- Lippiello, E., de Arcangelis, L., and Godano, C. 2010, *A&A* 511, L2.
- Lu, E.T. 1995, *ApJ* 447, 416
- Mason, J.P. and Hoeksema, J.T. 2010, *ApJ* 723, 634
- Metcalf, T.R., Jiao, L., Uitenbroek, H., McClymont, A.N., and Canfield, R.C. 1995, *ApJ* 439, 474
- Nishizuka, N., Sugiura, K., Kubo, Y., et al. 2017, *ApJ* 835, 156

- Pesnell, W.D., Thompson, B.J., and Chamberlin, P.C. 2011, *SoPh* 275, 3.
- Priest, E.R. 2014, *Magnetohydrodynamics of the Sun*, Cambridge: Cambridge University Press
- Rosner, R. and Vaiana, G.S. 1978, *ApJ* 222, 1104
- Sandman, A., Aschwanden, M.J., DeRosa, M., Wülser, J.P., Alexander, D. 2009, *SoPh* 259, 1.
- Sandman, A.W., Aschwanden, M.J. 2011, *SoPh* 270, 503.
- Schrijver, C.J., DeRosa, M.L., Title, A.M., and Metcalf, T.R. 2005, *ApJ* 628, 501
- Schrijver, C.J. 2007, *ApJ* 655, L117.
- Schrijver, C.J. 2016, *ApJ* 820, 103
- Strugarek, A. and Charbonneau, P. 2014, *SoPh* 289, 4137
- Sun, X., Hoeksema, J.T., Liu, Y., Kazachenko, M., and Chen, R. 2017, *ApJ* 839:67
- Sun, X., Hoeksema, J.T., Liu, Y., Wiegelmann, T., Hayashi, K., Chen, Q., et al. 2012, *ApJ* 748, 77
- Thalmann, J.K., Tiwari, S.K., and Wiegelmann, T. 2014, *ApJ* 780:102
- Thalmann, J.K., Linan, L., Pariat, E., and Valori, G. 2019, *ApJ* 880:L6
- Török, T., Kliem, B., and Titov, V.S. 2003, *A&A* 413, L27
- Wang, W., Liu, R., Wang, Y., Hu, Q., Shen, C., Jiang, C., and Zhu, C. 2017, *Nature Communications*, 8, 1330.
- Warmuth, A., and Mann, G. 2016a, *A&A* 588, A115
- Warmuth, A., and Mann, G. 2016b, *A&A* 588, A116
- Warren, H.P., Crump, N.A., Ugarte-Urra, I., Sun, X., Aschwanden, M.J., and Wiegelmann, T. 2018, *ApJ* 860, 46
- Wheatland, M.S., Sturrock, P.A., and McTiernan, J.M. 1998, *ApJ* 509, 448
- Wheatland, M.S. 2000, *ApJ* 532, 1209.
- Wheatland, M.S. Sturrock, P.A. and Roumeliotis, G. 2000, *ApJ*, 540, 1150.
- Wiegelmann, T. 2004, *SoPh* 219, 87
- Wiegelmann, T., Inhester, B., and Sakurai, T. 2006, *SoPh* 233, 215.
- Wiegelmann, T., Thalmann, J.K., Inhester, B., Tadesse, T., Sun, X., Hoeksema, J.T. 2012, *SoPh* 281, 37
- Wiegelmann, T., Neukirch, T., Nickeler, D.H., et al. 2017, *ApJSS* 229, 18
- Zhu, X.S., Wang, H.N., Du, Z.L., et al. 2013, *ApJ* 768, 119
- Zhu, X.S. and Wiegelmann, T., 2018, *ApJ* 866, 130

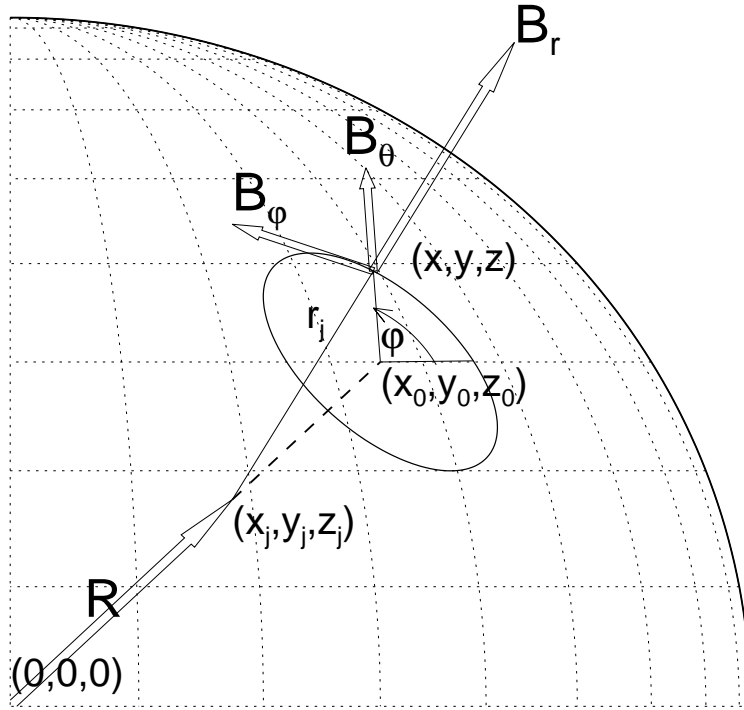


Fig. 1.— The geometry of the 3-D magnetic field components $B = (B_r, B_\phi, B_\theta)$ in a coronal position (x, y, z) is shown, computed from a magnetic charge j that is buried at a subphotospheric position (x_j, y_j, z_j) and is helically twisted by an azimuth angle ϕ . The origin $(0,0,0)$ of the spherical coordinate system is in the center of the Sun. The central twist axis (dashed line) intersects an equi-potential surface at position (x_0, y_0, z_0) . The radial field component B_r points radially away from the point charge at position (x_j, y_j, z_j) . The azimuthal magnetic field component B_ϕ at location (x, y, z) is orthogonal to the radial component B_r , and the poloidal field component B_θ is orthogonal to both the radial component B_r and the azimuthal component B_ϕ .

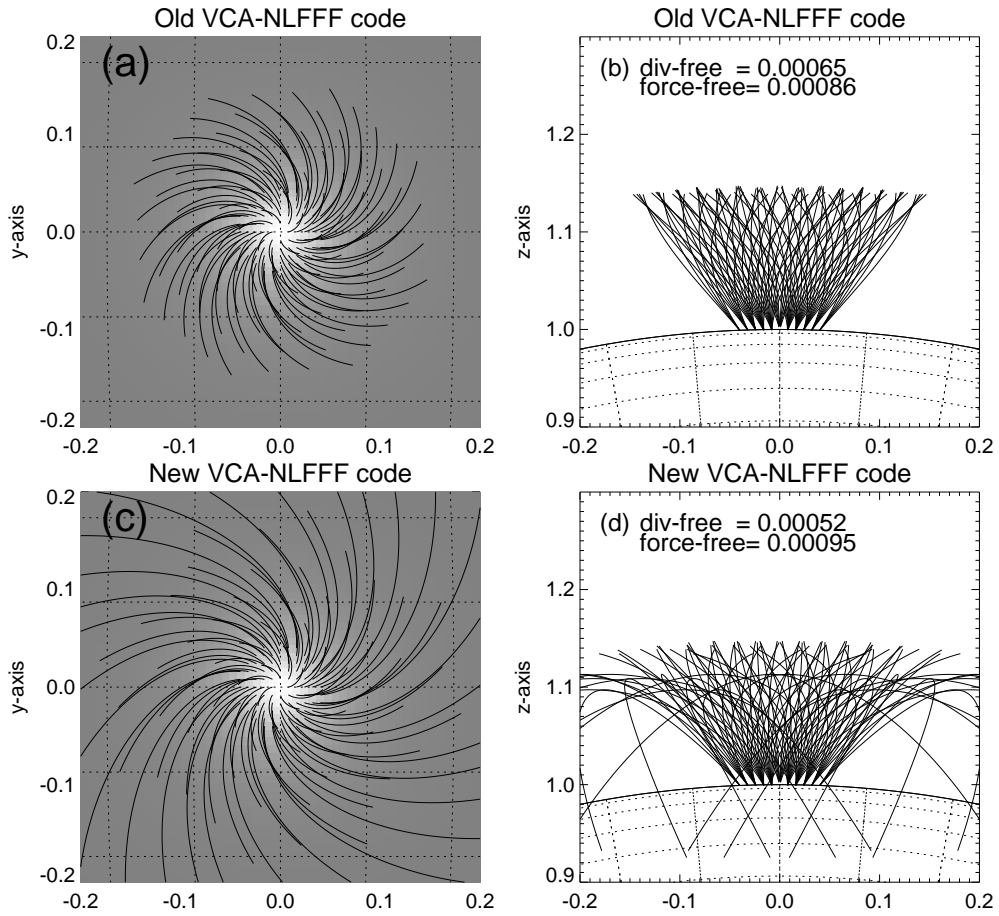


Fig. 2.— The magnetic non-potential field of a helically twisted sunspot is computed with the old VCA-NLFFF code (top panels) and with the new VCA3-NLFFF code (bottom panels), shown from a top view (left panels) and a side view (right panels). Note that the new field lines exhibit a curvature of the poloidal component B_θ (bottom right), which is neglected in the old code (with $B_\theta = 0$) (top right panel).

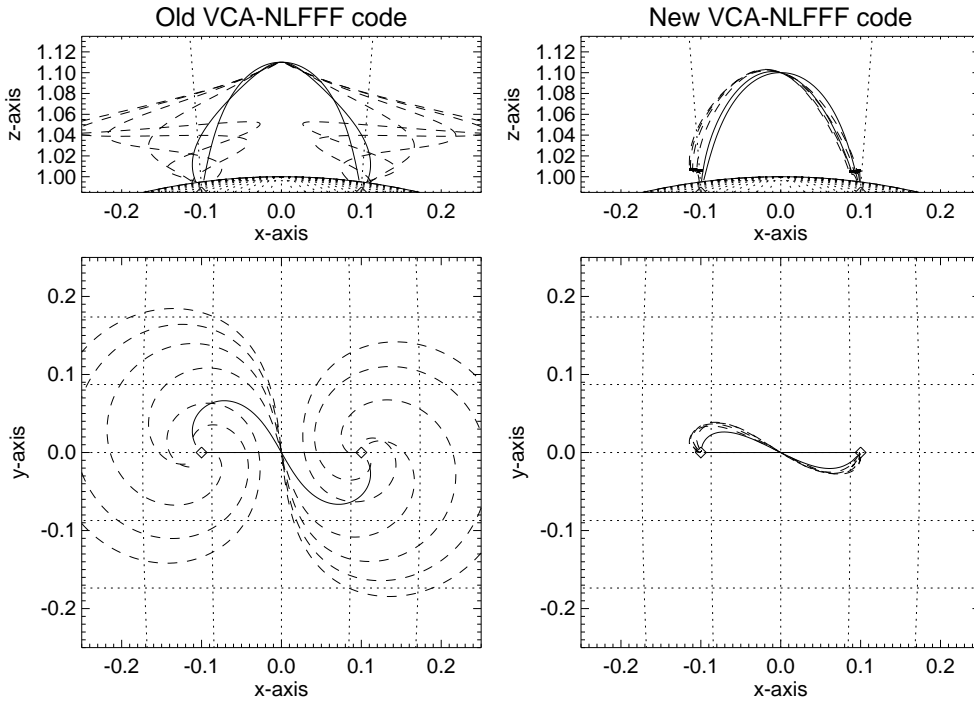


Fig. 3.— The non-potential magnetic field of a Gold-Hoyle flux rope with 1 to 5 helical windings (dashed curves) and the corresponding potential field solutions (solid) curves) are shown for the old VCA-NLFFF code (left panels) and the new VCA3-NLFFF code (right panels). Note that the neglect of the poloidal component ($B_\theta = 0$) leads to distorted field lines in calculations with the old VCA-NLFFF code, which are absent in the new VCA3-NLFFF code (right panels), where force-free solutions are found always to have less than one full turn of helical twist.

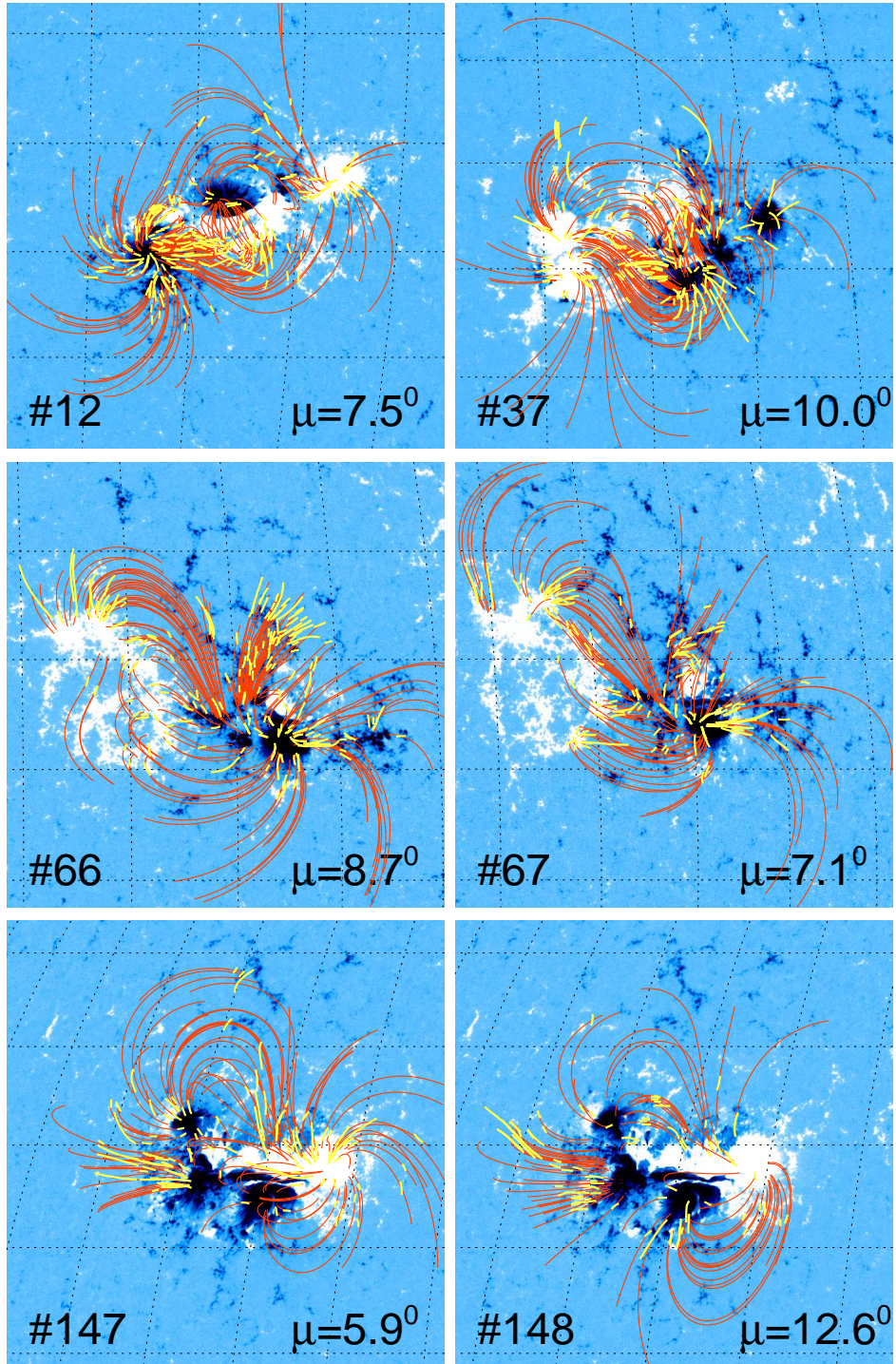


Fig. 4.— The HMI/SDO line-of-sight magnetogram (blue image) with positive (white) and negative (black) magnetic polarities is shown, along with automatically traced coronal loops (yellow segments) and theoretical magnetic field lines (red curves) that are computed with the VCA3-NLFFF code and intersect the traced loop segments at their midpoint, for 6 X-class flares observed with SDO. **The misalignment angle between the best-fit magnetic field model and observed loops is indicated with μ_2 .**

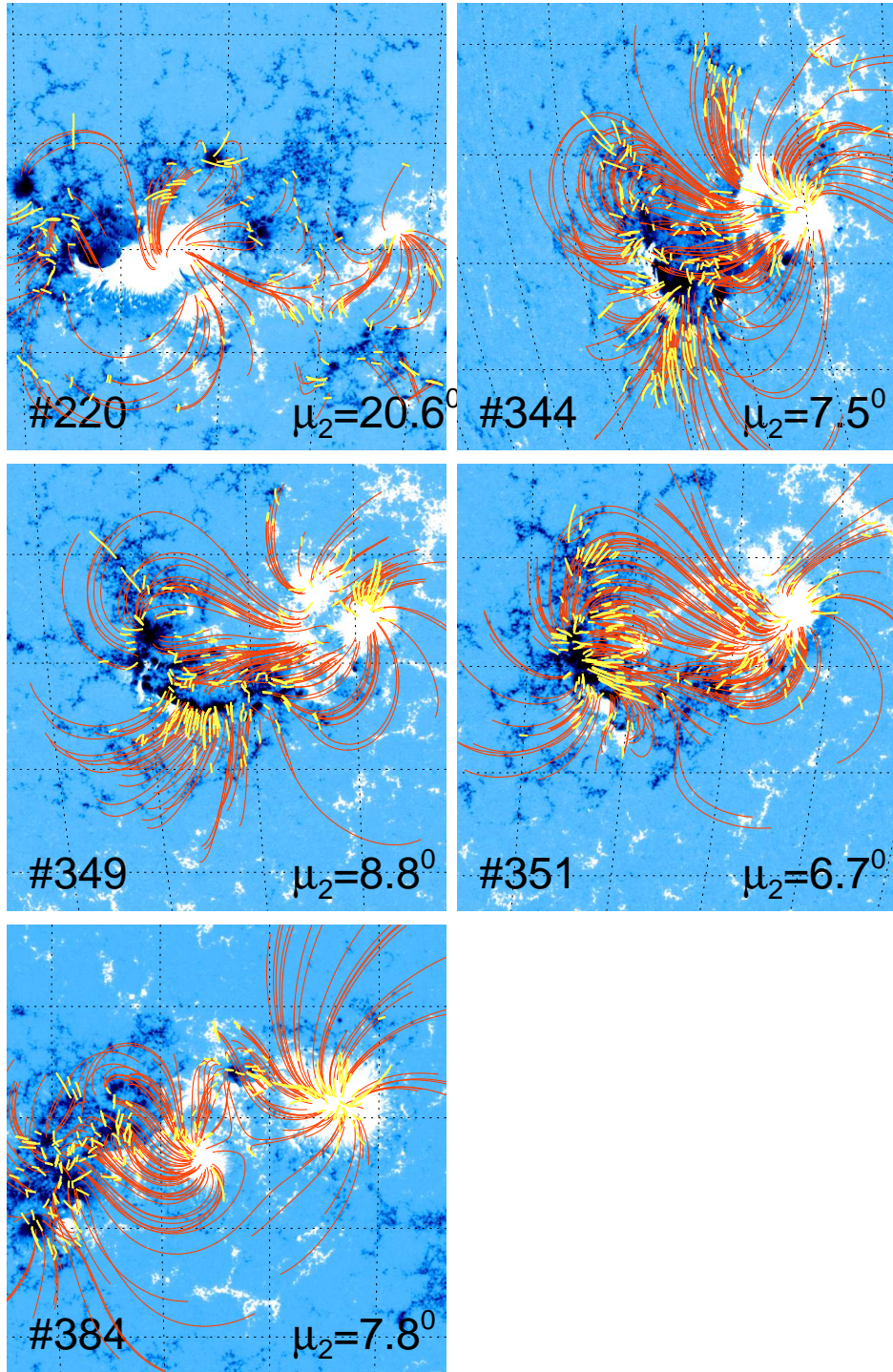


Fig. 5.— Similar representation as in Fig. 4, for 5 additional X-class flares.

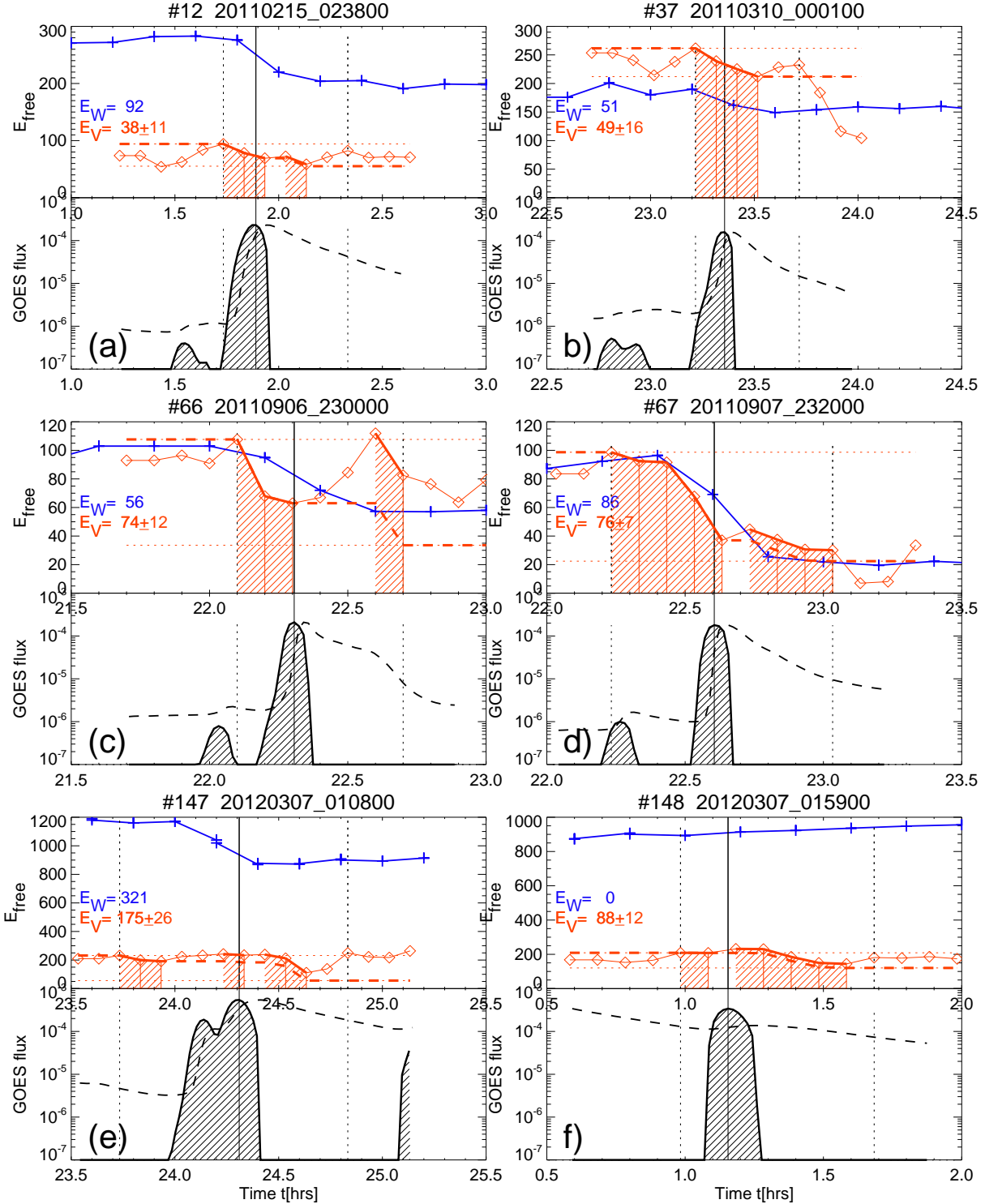


Fig. 6.— *Top panels:* Time evolution of free energy for 6 X-class flares, computed with the VCA3-NLFFF code (red), and compared with the Wiegelmann code (blue). Additionally we show the cumulative energy decrease function (dashed red curve and hatched areas), the dissipated energy E_V from the VCA3-NLFFF code, and E_W from the Wiegelmann code, the flare start and end time (vertical dotted lines), the peak time of the GOES flux profile time derivative. *Bottom rows of panels:* The GOES flux profile (dashed curve) and its time derivative (black hatched area).

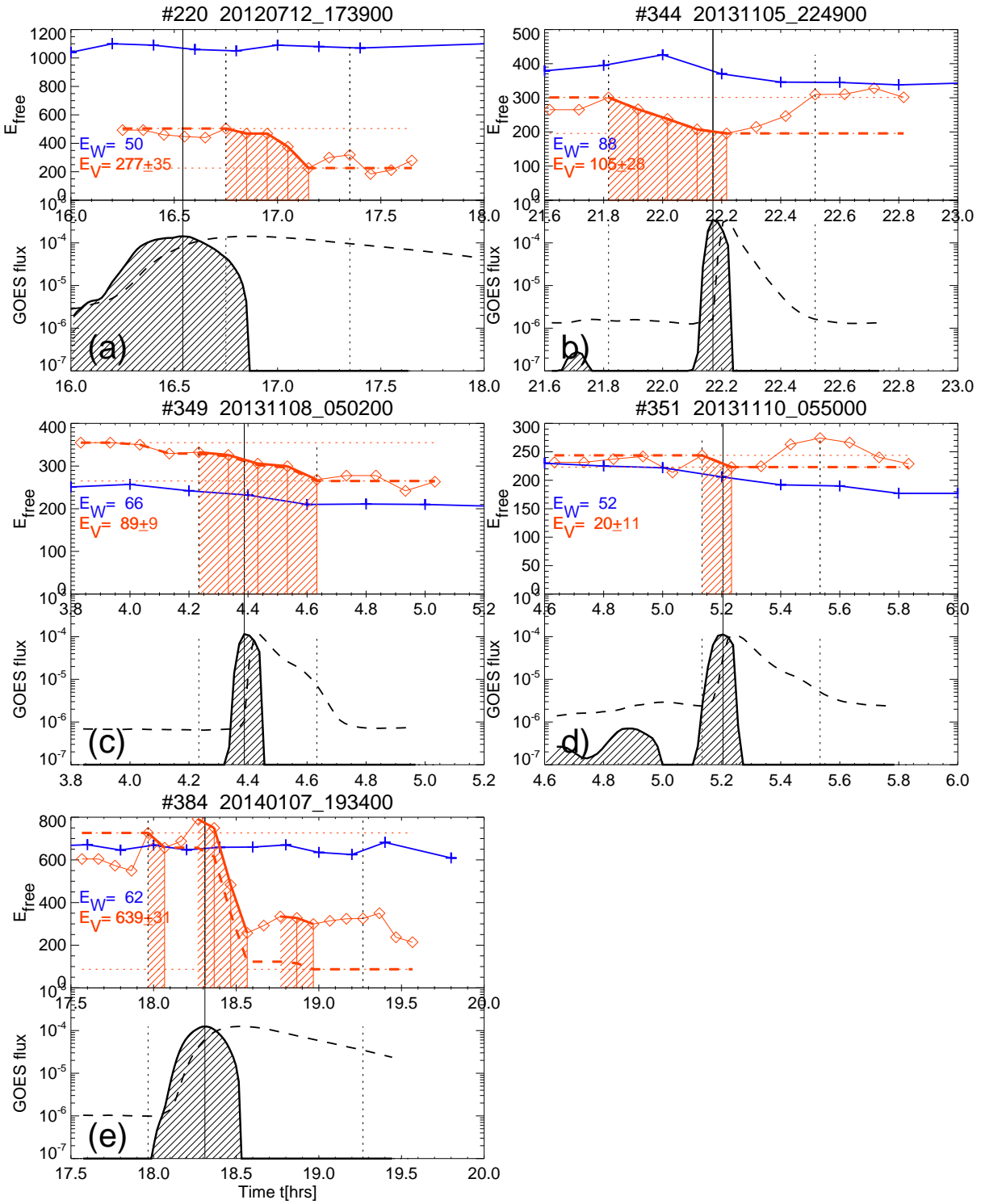


Fig. 7.— Similar representation as in Fig. 6, for 5 additional X-class flare events.

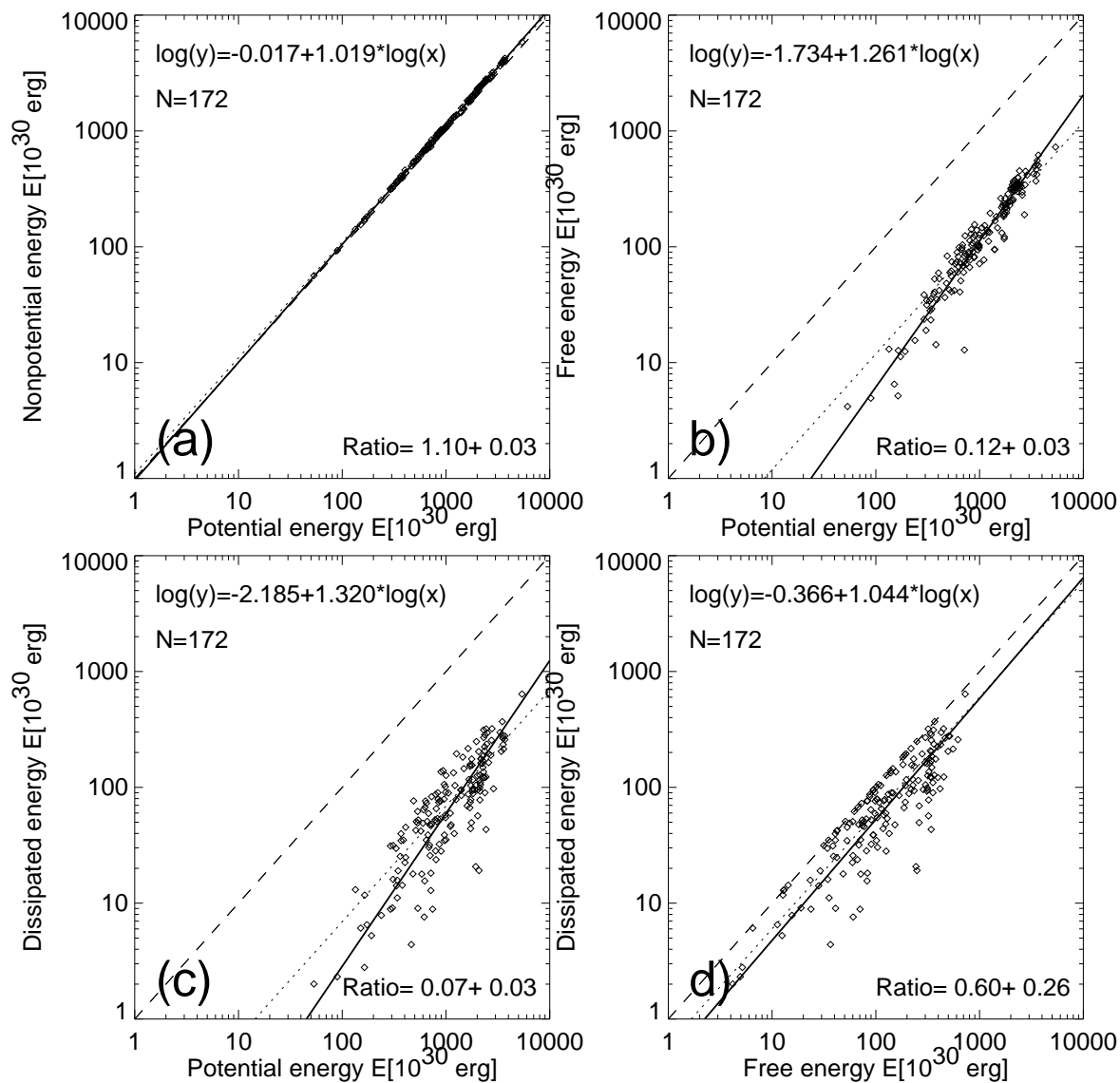


Fig. 8.— Scatterplots of potential, nonpotential, free, and dissipated magnetic energies of our analyzed sample with 173 M- and X- GOES class flare events. Linear regression fits in log-log space are indicated with thick black lines, constant ratios with dotted lines, and equivalence with dashed lines.

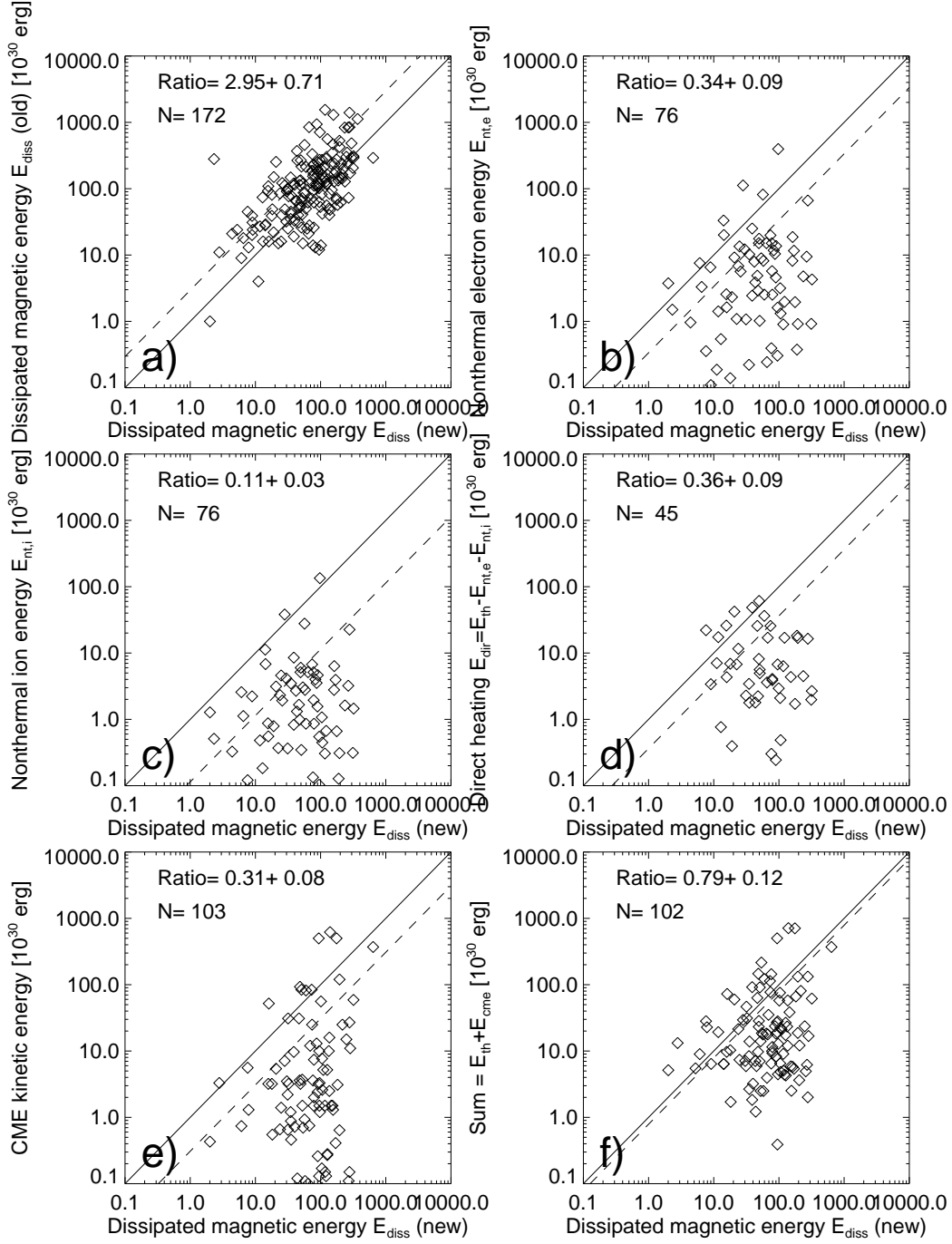


Fig. 9.— Scatterplot of the various forms of energies: dissipated magnetic energies E_{diss}^{old} (a), nonthermal electron energies $E_{nt,e}$ (b), nonthermal energies in ions $E_{nt,i}$ (c), direct heating $E_{dir} = E_{th} - E_{nt,e} - E_{nt,i}$ (d), CME kinetic energy E_{cme} (e), and the sum of primary energies $E_{sum} = E_{nt,e} + E_{nt,i} + E_{dir} + E_{cme} = E_{th} + E_{cme}$ (f), as a function of the dissipated magnetic energy E_{diss} obtained with the new improved code. Note that energy closure within $E_{sum}/E_{diss} = 1.04 \pm 0.21$ is obtained for 44 events that have complete data (f).

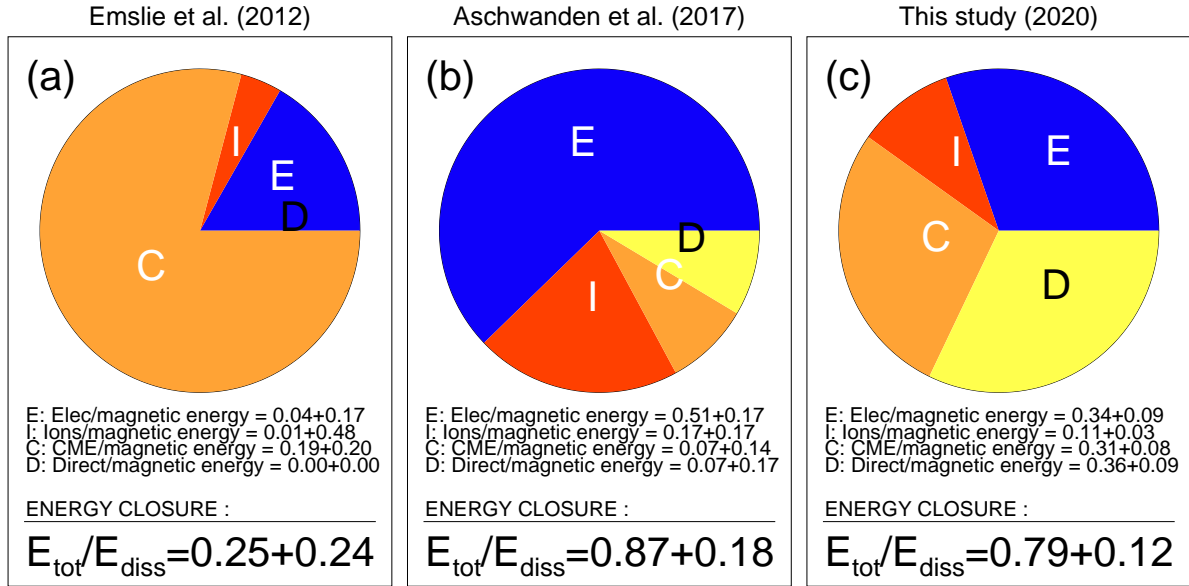


Fig. 10.— Occurrence frequency distributions of energy parameters (histograms) with power law fits in log-log space (solid line). The error of the slope a is defined by a/\sqrt{n} , and the total energy integrated over the entire distribution is indicated with E_{tot} . Note that the slopes have typical values of $a \approx 1.4 - 1.9$.

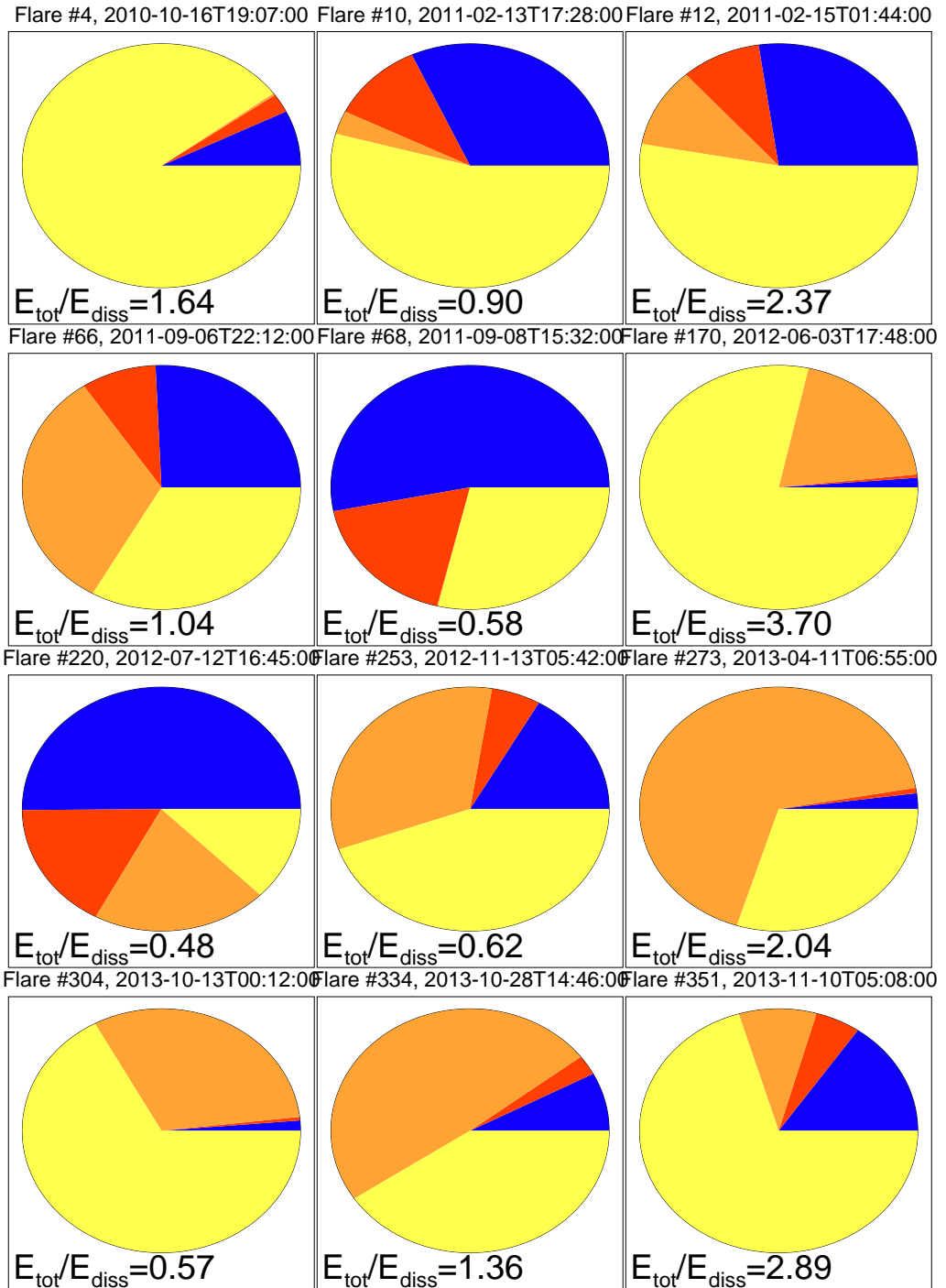


Fig. 11.— Pie chart diagrams the energy ratios of electrons (blue), ions (red), CMEs (orange), and direct heating (yellow) as a fraction of the total dissipated magnetic energy, for the data set of Emslie et al. (2012) (left panel), our earlier work (Aschwanden et al. 2017) (middle panel), and the present study (right panel).

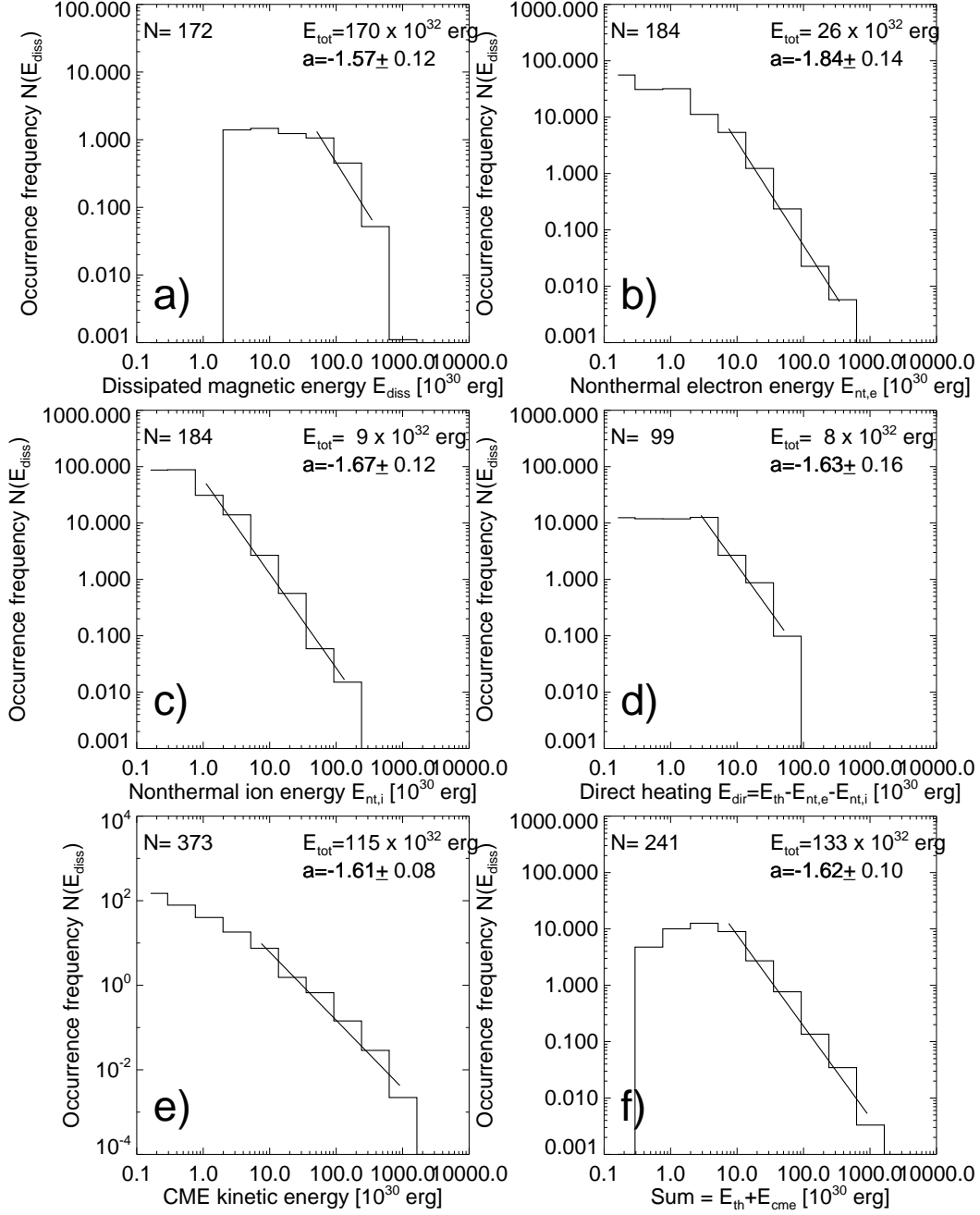


Fig. 12.— Pie chart diagrams the energy ratios of electrons (blue), ions (red), CMEs (orange), and direct heating (yellow) as relative fractions, shown for 12 flares. The ratios of the total energy $E_{tot} = E_{th} + E_{cme}$ to the total dissipated magnetic energy E_{diss} is given in the lower left corners.

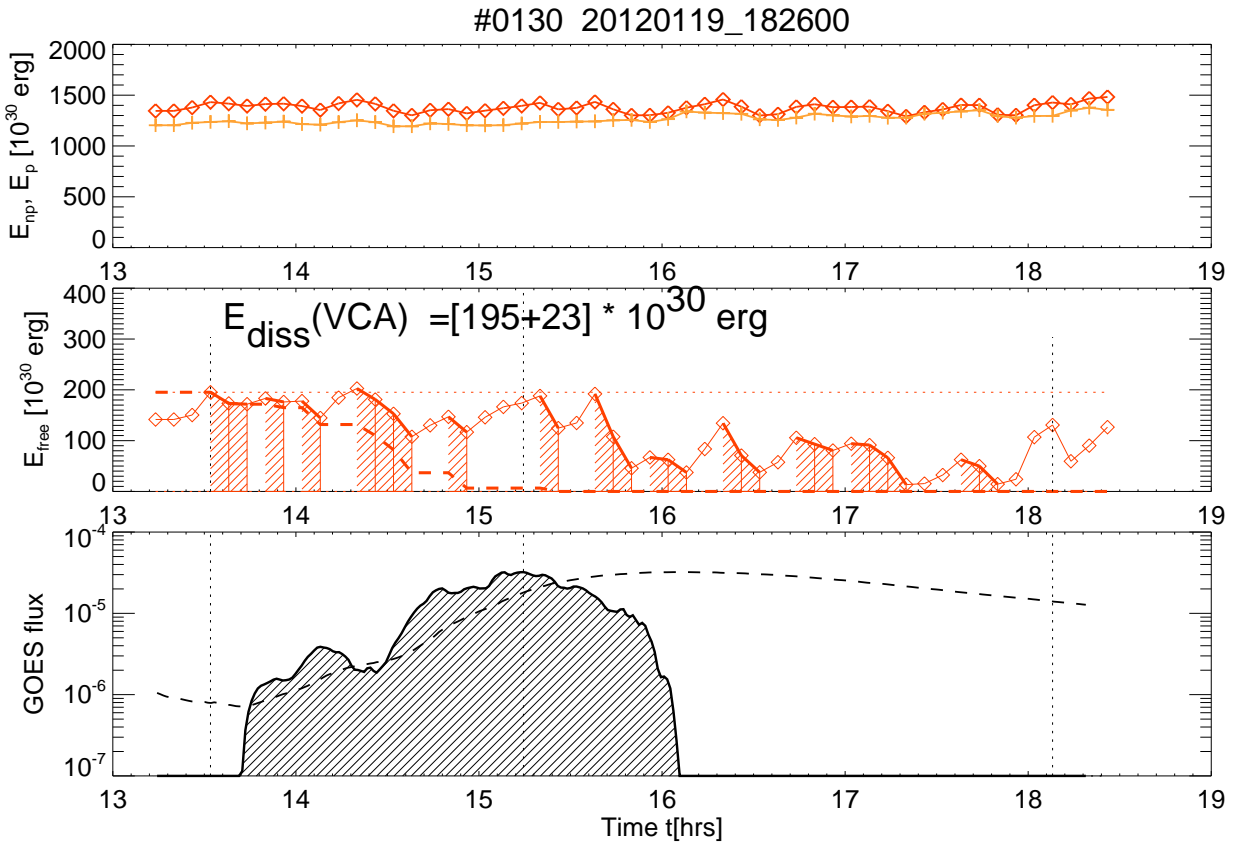


Fig. 13.— Time evolution of potential and non-potential energies (top panel), the free energy (thick red curve in second panel), time intervals of energy decreases (hatched red areas), cumulative free energy decrease function (dashed curve in middle panel), GOES 1-8 Å flux (dashed curve in bottom panel), and time derivative of GOES flux (hatched black areas in bottom panel), for the long-duration flare #130 on 2012-Jan-19, 18:26 UT, which lasted over 4 hrs.